ETH
Eidgenössische Technische Hochschule Zürich
Swiss Federal Institute of Technology Zurich

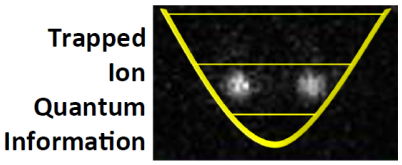

ETH Zurich, Department of Physics

Spectral filtering and laser diode injection for multi-qubit trapped ion gates

Master Thesis

Supervisor:

Christa Flühmann
Prof. Dr. Jonathan Home

Student:

Lukas Gerster

August 2015

Abstract

The 729 nm laser used to address the $|4^2S_{1/2}, m_j = \frac{1}{2}\rangle \leftrightarrow |3^2D_{5/2}, m_j = \frac{3}{2}\rangle$ quadrupole transition of $^{40}\,Ca^+$ which is used to define a qubit has undesirable spectral components at $\approx \pm 1.5\,\mathrm{MHz}$ of the center frequency due to the stabilization system.
In order to remove those components, the light was filtered using a high-finesse cavity. $50\,\mu\mathrm{W}$ of light were transmitted through the cavity, which were subsequently amplified to $45\,\mathrm{mW}$ by injecting a laser diode.
A phase lock to a second laser was set up to allow work around the high finesse cavity. The injection characteristics of two different diodes were investigated and the spectrum of the amplified light was measured using the ion as reference. The temperature dependence of the transmission lines of the cavity were determined. A scheme for cancelling noise introduced by optical fibers is described.

Contents

Acknowledgements

I would like to thank Christa Flühmann for supervising me, always taking time for my questions, her tips and hints as well as many interesting discussions.
Further I would like to thank Robin Oswald, who helped me a lot with the theory of phase locked loops, Alex Hungenberg for his help with setting up the datalogger, Daniel Kienzler for his knowledge about fibers, optics and ion trapping in general, Hsiang-Yu Lo and Chiara Decaroli who invested their time to proof read my thesis.
I also want to thank everyone else in the TIQI group who helped me with their explanations and showed patience with 729 laser interruptions.
I would like to thank Prof. Jonathan Home for the opportunity to do my Master thesis in the TIQI group, I very much enjoyed my time in the group, and it was a pleasure to work with you all.

Chapter 1

Introduction

The difficulties in simulating quantum mechanical systems on classical computers led Richard Feynman to propose the use of a computer working on quantum mechanical principles [1]. Later algorithms were found that would enable a quantum computer to perform certain tasks more efficiently than any possible classical computer, such as factorizing large numbers (Shor's Algorithm [2]) or searching a database (Grover's Algorithm [3]).
In 1995 Cirac and Zoller first proposed (See [4]) to use trapped ions to implement a two qubit gate, which is a key element to realize universal quantum computing [5], using internal electronic states of ions as qubits and vibrational states to couple multiple qubits together.
The coupling of internal and vibrational states requires the capability to address transitions that both involve changing the internal state and the quantized vibrational states of motion called sideband transitions. To address these transitions the laser is detuned by typically a few MHz. The coupling strength for the sideband transitions is much lower than for the carrier transition which only involves internal states of the ion alone. Qubit operations that use the sideband transitions are thus sensitive to noise in the laser spectrum driving unwanted carrier transitions, reducing the fidelity of the gate.
In this thesis a setup is described to filter the spectral components that are produced by the servo stabilizing the laser frequency. These spectral components called servo bumps severely restrict the ability to perform multi-qubit gates which rely on the sidebands, but are unavoidable without compromising the stability of the laser or the linewidth.
To solve this problem the high finesse cavity to which the laser is locked is used as a spectral filter. As the laser power that can be coupled into the cavity is limited, the light transmitted through the cavity is then sent to a laser diode which is injection locked in order to achieve sufficient power for seeding a tapered amplifier, which finally amplifies the light to the power required for the experiments.

Chapter 2

Control of Ions

2.1 Rabi Oscillations

An ion confined in a trap has both motional and internal degrees of freedom. At the bottom of the potential well the trap potential is engineered to be approximately harmonic, where the frequency along one axis (axial mode) is lower than the frequency along the other two (radial modes). Considering only the axial mode of motion and two internal states the ion can be described by the product of a two level system and a harmonic oscillator,

$$H = H_0 + H_{osc} \tag{2.1.1}$$

$$= \hbar\omega_{eg}\sigma_z + \hbar\omega_{osc}(a^\dagger a + 1/2). \tag{2.1.2}$$

The states can be written as a product of harmonic oscillator states and the two internal states

$$\psi(t) = \sum_{s=e,g}\sum_{n=0}^{\infty} c_{s,n}(t)|s\rangle|n\rangle \tag{2.1.3}$$

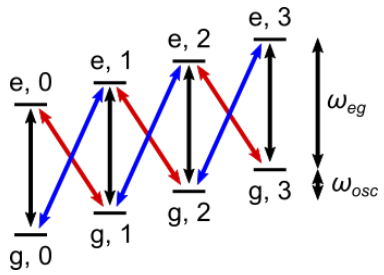

Figure 2.1.1: Energy levels for an ion with two internal states with energy difference $\hbar\omega_{eg}$ and one motional mode with energy spacing $\hbar\omega_{osc}$. The arrows show the carrier and the first red and blue sideband transitions.

Transitions between the states of this system can be driven applying a laser to the ion. Approximating the laser as a classical electromagnetic field oscillating at a single frequency gives an interaction Hamiltonian

$$H_{int} = \hbar\Omega_0(\sigma_+ + \sigma_-)(e^{i(kz-\omega t+\phi)} + e^{-i(kz-\omega t+\phi)}) \tag{2.1.4}$$

where $\Omega_0 \propto E$ is the interaction strength, E is the strength, ω the frequency and ϕ the phase of the applied field and z is the position operator along the axial direction. The proportionality factor of the interaction strength for quadrupole transitions depends both on angle and polarization of the laser beam relative to an applied magnetic field on the ion (For a detailed treatment see [6]).
Going to an interaction picture and making a rotating frame approximation by neglecting rapidly oscillating $\exp(\pm i(\omega + \omega_{eg}))$ terms, one gets [7]

$$H'_{int} = \hbar\Omega_0\sigma_+ \exp(i[\eta(ae^{-i\omega_{osc}t} + a^\dagger e^{i\omega_{osc}t}) - \delta t + \phi]) + h.c., \tag{2.1.5}$$

where $\delta = \omega - \omega_{eg}$ is the detuning and η is the Lamb-Dicke parameter. The states are chosen to be long lived so they are well resolved. Further the laser is tuned such that $\delta = (n - n')\omega_{osc} + \Delta$ with $\Delta \ll \omega_{osc}, \Omega_0$ and n, n' integers. This corresponds to the laser being close to resonant with some transition.
Three types of transition are of special interest, the carrier transition ($n' = n$), the first red sideband ($n' = n - 1$) and the first blue sideband ($n' = n + 1$) On resonance we find that state $|g, n\rangle$ evolves as

$$\psi(t) = \cos(\Omega_{n',n}t/2)|g, n\rangle + e^{i\phi}\sin(\Omega_{n',n}t/2)|e, n'\rangle \tag{2.1.6}$$

The transition frequency $\Omega_{n',n}$ is called the Rabi frequency. If the Lamb-Dicke criterion is satisfied the interaction Hamiltonian can be expanded in η. The condition of $\eta^2 n(n+1) \ll 1$ corresponds to the condition that the spatial extension of the harmonic oscillator wave function id small compared to $\lambda/2\pi$, where λ is the wavelength of the laser light applied to the ion.
The Rabi frequency is then given for the carrier and the sidebands [7] by

$$\Omega_{n,n} = \Omega_0 \tag{2.1.7}$$

$$\Omega_{n+1,n} = \Omega_0\eta\sqrt{n+1} \tag{2.1.8}$$

$$\Omega_{n-1,n} = \Omega_0\eta\sqrt{n} \tag{2.1.9}$$

As we assume we are in the Lamb-Dicke regime where $\eta^2(2n+1) \ll 1$ the Rabi frequency of the sideband transitions is much lower than the carrier transition for the same strength of the electromagnetic field. When we address the sideband transitions we are thus very sensitive to noise also driving the carrier transition. If the laser is not exactly on resonance, the transition probability from $|g, n\rangle$ to $|e, n'\rangle$ is modified to [8]

$$p_{|e,n'\rangle} = \frac{\Omega_R^2}{\Omega^2}\sin^2(\Omega t/2), \tag{2.1.10}$$

where $\Omega^2 = \Omega_R^2 + \Delta^2$. For a detuned beam the Rabi oscillations thus get faster, but the amplitude is reduced.

2.2 Multi-Qubit Gates

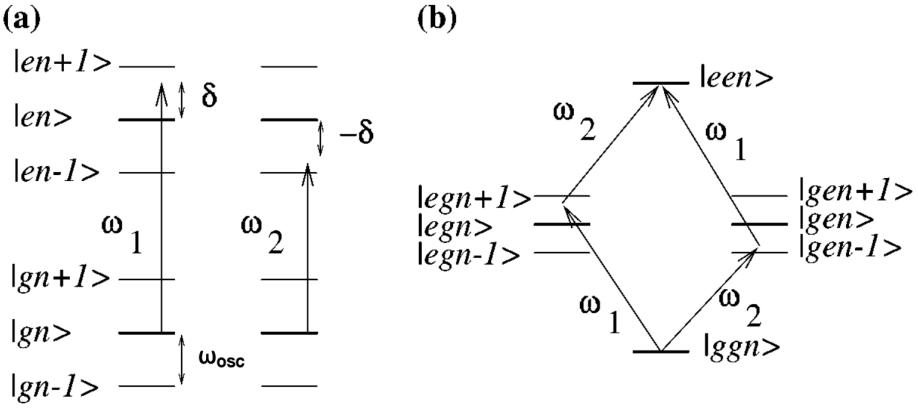

Figure 2.2.1: Level scheme for Mølmer-Sørensen gate. (a) shows the chosen laser frequencies relative to the energy levels of each ion, (b) shows the two paths possible for the combined two ion system. Figure from [9]

For a working quantum computer several requirements have to be fulfilled. David DiVicenzo stated his seven criteria [5] that have to be fulfilled for a quantum computer architecture. One criterion requires a complete set of quantum gates. This criterion can be fulfilled with a set of single qubit operations and a two qubit cNOT gate. As it is very difficult to couple the electronic states of ions directly, schemes for gates involving multiple ions make use of the common motional states of the ions [4].
One gate of particular interest is the gate proposed by Sørensen and Mølmer [9]. In this scheme two laser beams are used, each shining on a single ion. The first ion is addressed with a detuning close to the upper sideband, and the second ion is addressed with a beam with a detuning equal to the negative of the first beam. This couples the states $|ggn\rangle \leftrightarrow \{|egn+1\rangle, |gen-1\rangle\} \leftrightarrow |een\rangle$, where e, g correspond to the excited or ground state of the first or second ion, n denotes the vibrational state of the ion in the trap (Fig. 2.2.1).
This system is described by the following Hamiltonian

$$H = H_0 + H_{int}, \tag{2.2.1}$$

$$H_0 = \hbar\omega_{osc}(a^\dagger a + \frac{1}{2}) + \hbar\omega_{eg}\sum_i \sigma_{zi}/2, \tag{2.2.2}$$

$$H_{int} = \sum_i \frac{\hbar\Omega_i}{2}(\sigma_+ e^{i[\eta_i(a+a^\dagger)-\omega_i t]} + \sigma_- e^{-i[\eta_i(a+a^\dagger)-\omega_i t]}), \tag{2.2.3}$$

where $a, a^\dagger$ are the ladder operators of the vibrational modes, ω_{osc} is the vibrational frequency, ω_{eg} is the transition frequency between the internal states of the ion, and ω_i, Ω_i is the laser frequency respectively the Rabi frequency of the

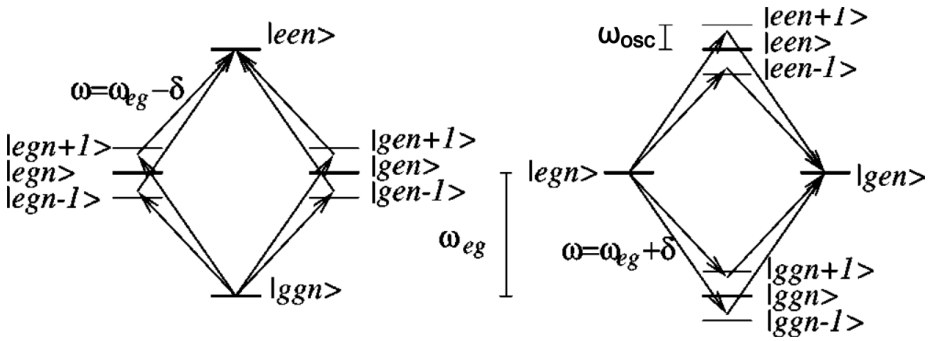

Figure 2.2.2: Level scheme for Mølmer-Sørensen gate using bichromatic light. The left image shows the possible paths connecting the states $|ggn\rangle$ and $|een\rangle$, the right image shows the transitions between $|gen\rangle$ and $|egn\rangle$. Figure from [10]

ith ion.
Assuming two ions with $\omega_{osc1} = \omega_{osc2} = \omega_{osc}$ and $\Omega_1 = \Omega_2 = \Omega$ and detunings selected as described above, the only allowed transitions are between $|ggn\rangle$ and $|een\rangle$. The Rabi frequency for this transition is then given by [9]

$$\widetilde{\Omega} = -\frac{(\Omega\eta)^2}{2(\omega_{osc} - \delta)}, \tag{2.2.4}$$

where δ is the detuning of the laser addressing the first ion.
This result is remarkable as it does not depend on the number state n the system is in, as the dependence is canceled out between the two possible paths the system can take to move from $|ggn\rangle$ to $|een\rangle$, either it can go over $|egn+1\rangle$ or $|gen-1\rangle$. The evolution of the internal states of the ion is thus decoupled from the motional state. It does not even require that the ions remain in the same n state during gate operation, thus making the operation insensitive to heating.
Unfortunately the states $|eg\rangle$ and $|ge\rangle$ do experience n dependent energy shifts, which introduce phase factors dependent on the motional state n, e.g. at the time $T = \frac{2\pi(\omega_{osc}-\delta)}{\mu^2\Omega^2}$ when the states $|gg\rangle$ and $|ee\rangle$ are inverted, factors of $(-1)^n$ will destroy the coherence between the states $|eg\rangle$ and $|ee\rangle$.
Coherence can be restored by changing the sign of the laser detuning after time $\frac{T}{2}$. This will lead to every phase component proportional to n to rotate in the opposite direction, and a revival of coherence at T
This trick is however sensitive to heating, as the phases will no longer cancel out if the vibrational quantum number n is not the same during the second half of the gate operation. If the detunings are instead inverted N times the error in phase will be only on the order of the phase error at timescale $\frac{T}{N}$.
Instead of changing the detuning of the lasers many times, lasers with both detunings can be applied to both ions simultaneously. Assuming opposite detunings and identical Rabi frequencies Ω there are two additional paths connecting $|ggn\rangle$ and $|een\rangle$ whose contribution is identical to the two paths already considered, leading to a doubling of the Rabi frequency $\widetilde{\Omega}$. The bichromatic light also

leads to transitions between the states $|gen\rangle$ and $|egn\rangle$ (Fig. 2.2.2). The Rabi frequency of this transition is the negative of the frequency of the transition between $|ggn\rangle$ and $|een\rangle$. In the weak field limit $\eta\Omega \ll \omega_{osc} - \delta$ the population transferred to the intermediate states can be neglected and the time evolution is described by

$$|gg\rangle \to \cos\Big(\frac{\widetilde{\Omega}T}{2}\Big)|gg\rangle + i\sin\Big(\frac{\widetilde{\Omega}T}{2}\Big)|ee\rangle \tag{2.2.5}$$

$$|ee\rangle \to \cos\Big(\frac{\widetilde{\Omega}T}{2}\Big)|ee\rangle + i\sin\Big(\frac{\widetilde{\Omega}T}{2}\Big)|gg\rangle \tag{2.2.6}$$

$$|ge\rangle \to \cos\Big(\frac{\widetilde{\Omega}T}{2}\Big)|ge\rangle - i\sin\Big(\frac{\widetilde{\Omega}T}{2}\Big)|eg\rangle \tag{2.2.7}$$

$$|eg\rangle \to \cos\Big(\frac{\widetilde{\Omega}T}{2}\Big)|eg\rangle - i\sin\Big(\frac{\widetilde{\Omega}T}{2}\Big)|ge\rangle \tag{2.2.8}$$

For stronger fields some population is transferred to the intermediary states with different n. This leads to some coupling between $|een\rangle, |ggn\rangle$ and $|gen\rangle, |egn\rangle$, however the parameters of the Hamiltonian can be tuned to still achieve full population transfer. A detailed description is given in [10].
This gate can be used together with single qubit operations to perform a cNOT gate, and thus single qubit gates and the Mølmer-Sørensen gate would fulfill the requirement of an universal set of quantum gates.

2.3 $^{40}Ca^{+}$ as qubit

There are multiple species of ions suitable, as well as multiple possible choices of states for a qubit. The qubit is then defined between the $4^2S_{1/2}$ $m = 1/2$ and $3^2D_{5/2}$ $m = 3/2$ states. The transition can be addressed with a 729 nm laser (Fig. 2.3.1). The transition between the states is a quadrupole transition, giving the upper state a long lifetime of 1.1 s.
A 119.4 G magnetic field is applied to the ion. The magnetic field lifts the degeneracy of the states due to the Zeeman splitting and defines the axis of quantization. The strength of the magnetic field is chosen for using the ion together with $^9Be^+$ where the qubit states are insensitive to magnetic field fluctuations in first order, giving rise to a long coherence time [12].
To actually use the qubit more states are required as well as lasers to address the transitions. The 397 nm addressing the fast $4^2S_{1/2} \leftrightarrow 4^2P_{1/2}$ dipole transition is used for detection as well as Doppler cooling. The 866 nm laser is used to repump the ion from the $3^2D_{3/2}$ state, and the 854 nm laser is used to reset the qubit.

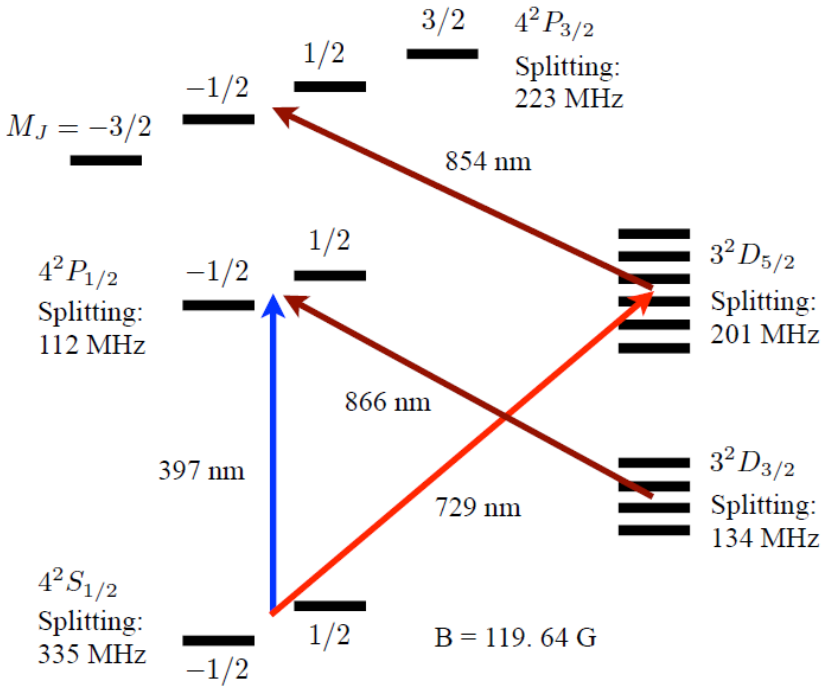

Figure 2.3.1: Scheme of the states and lasers used for implementing a $^{40}Ca^{+}$ qubit. Figure from [11]

Chapter 3

Frequency Stabilization of Lasers

3.1 Phase Locked Loop

3.1.1 Open Loop Transfer function

Free running diode lasers do not have narrow enough linewidths and the required frequency stability to be used for controlling qubits. Both linewidth and stability can be improved by locking the laser to an external reference like a cavity (See Sec. 3.2) or to another laser (See Sec. 3.3). To stabilize frequencies a phase locked loop (PLL) is employed.
The simplest scheme consists of a phase detector, a controller, a variable frequency oscillator and a feedback path (Fig. 3.1.1). The components can be described in Laplace transform domain,

$$\theta_o = F(s)\mathrm{VFO}(s)\theta_d \tag{3.1.1}$$

$$\theta_d = K_d(\theta_i - \theta_o), \tag{3.1.2}$$

where VFO(s) is the transfer function of the variable frequency oscillator, $F(s)$ the transfer function of the controller, θ_o the output signal, θ_i the input signal and θ_d the signal at the detector in the Laplace domain. K_d is the gain multiplier of the detector.
As the phase is the time derivative of the frequency the VFO can be seen as integrator of the phase and therefore has a transfer function

$$\mathrm{VFO}(s) = \frac{V}{s}, \tag{3.1.3}$$

where V is the gain of the VFO. As $F(s)$ we take a controller with a proportional and an integral part. The controller then has transfer function

$$F(s) = K_P + \frac{K_I}{s}, \tag{3.1.4}$$

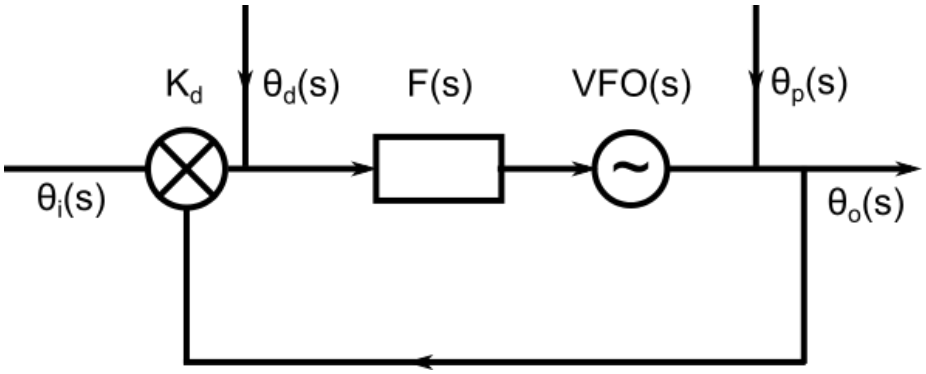

Figure 3.1.1: Simple phase locked loop consisting of phase detector K_d, controller $F(s)$ and variable frequency oscillator VFO(s). Noise can enter the loop either via the detector θ_d or the process θ_p.

with K_P the gain of the proportional path and K_I the gain of the integrator path.
The open loop transfer function describes the response of the system without a feedback path. It is given by

$$G(s) = K_d F(s)\mathrm{VFO}(s) = K_d \left(K_P + \frac{K_I}{s} \right) \frac{V}{s}. \tag{3.1.5}$$

3.1.2 Closed Loop Transfer function

The response of the closed loop can be written as function of the open loop response. This system transfer function $H(s)$ describes how the loop follows a change in the reference. It is given by

$$H(s) = \frac{\theta_o}{\theta_i} = \frac{G(s)}{1 + G(s)}. \tag{3.1.6}$$

The system transfer function determines a phase locked loops ability to follow a change in the reference signal. It also describes the response of the loop to detector noise as it is indistinguishable to a change in the reference.
The effect of process noise θ_p in the output on the loop can be described by the error transfer function $E(s)$ [13]

$$E(s) = \frac{\theta_o}{\theta_p} = \frac{1}{1 + G(s)}. \tag{3.1.7}$$

Process noise are fluctuation in the loop that can come from either the controller or the VFO.
The system and the error transfer function are connected by the relation

$$H(s) + E(s) = 1 \tag{3.1.8}$$

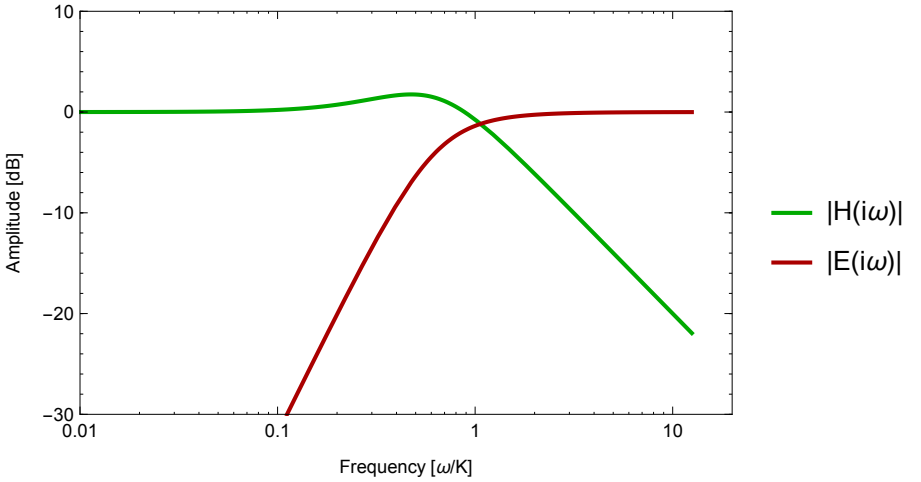

Figure 3.1.2: Example Bode plot (frequency response) of the magnitude of system response and error function normalized to the gain frequency with damping $\zeta = 0.8$ and no time delay.

Putting the expression for $G(s)$ into the system transfer function we get

$$H(s) = \frac{VK_d(sK_P + K_I)}{s^2 + sVK_PK_d + VK_IK_d} \tag{3.1.9}$$

We can reduce the number of parameters as the behavior of the loop can be described by only two parameters, the open loop gain and the damping

$$K = K_dVK_P, \quad \zeta = \frac{K_P}{2}\sqrt{\frac{K_dV}{K_I}}, \tag{3.1.10}$$

giving a system transfer function of

$$H(s) = \frac{(Ks + \frac{K^2}{4\zeta^2})}{s^2 + (Ks + \frac{K^2}{4\zeta^2})} \tag{3.1.11}$$

and a corresponding error transfer function

$$E(s) = \frac{1}{s^2 + (Ks + \frac{K^2}{4\zeta^2})} \tag{3.1.12}$$

The frequency response can be calculated by setting $s = i\omega$. Fig. 3.1.2 shows the amplitude of the frequency response. The system response function is approximately constant up to K, giving the frequency range in which the servo can follow the reference, higher frequencies are suppressed. The error function in comparison is lower than 0 dB below K, here the servo suppresses process

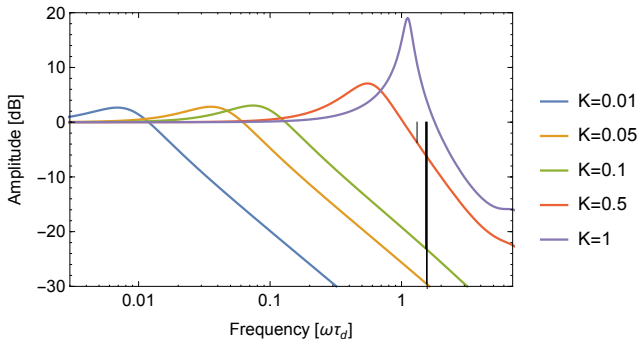

(a) Magnitude Response

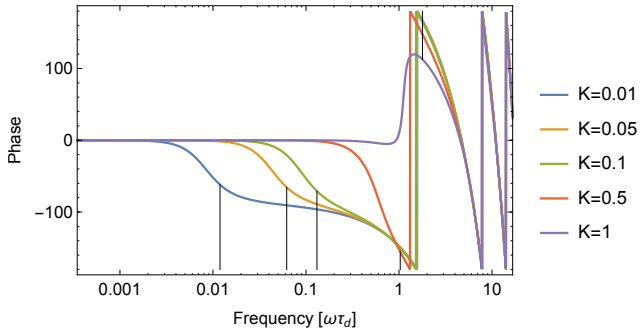

(b) Phase Response

Figure 3.1.3: Bode plot of system transfer function for different values of gain with fixed time delay. With increasing gain values the gain margin is reduced, until the system becomes unstable. Similarly the phase margin is reduced for high gain values.

noise (Fig. 3.1.5). This feature is what we are interested in for stabilization, as our reference has little low frequency noise compared to our free running process. With the phase locked loop the output is thus dominated by the reference and no longer the process noise. Noise at frequencies higher than K cannot be suppressed.
These properties make it reasonable to use the gain K as a measure of the bandwidth of a controller [14], however other definitions are also commonly used.

3.1.3 Loop Stability

There are several possible criteria for determining if a closed loop is stable or not. One criterion is the Bode criterion which states that a system with a stable open loop the closed loop will be stable if the phase $\mathrm{Arg}[H(i\omega_c)]$ of the system transfer function is less than 180° at the gain crossover frequency ω_c which ful-

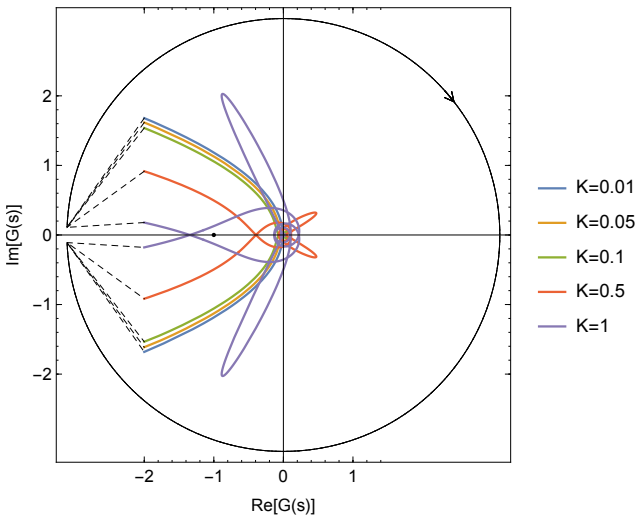

Figure 3.1.4: Nyquist plot of the open loop transfer function. The contour with $K = 1$ circles -1, rendering the corresponding closed loop unstable.

fills $|H(i\omega_c)| = 1$. If this is not the case, the frequency component where the phase shift is $-180°$ is infinitely amplified, unlocking the loop [14].
The gain margin is the gain difference to 1 at the frequency where the phase shift is $-180°$ ($g_g = 1/H(i\omega_\pi)$), while the phase margin is the phase difference to $-180°$ at the gain crossover frequency ($g_p = \mathrm{Arg}[H(i\omega_p)] + 180°$). These margins give the robustness of the lock (Fig. 3.1.3).
The Nyquist criterion states that the closed loop $H(s) = G(s)/(1 + G(s))$ is stable if the open loop is stable and the contour $G(i\omega)$ of the open loop transfer function plotted in the complex plane does not encircle the point -1 (See Fig. 3.1.4) [13].
From this plot the stability margin can be read off, which is defined as $g_s = \mathrm{Min}_\omega[1 + G(i\omega)]$.
A second order phase locked loop without time delays is unconditionally stable for arbitrarily large values K. In real systems there is always a time delay present, which can be included by introducing a delay term

$$\Lambda(s) = e^{-s\tau_d} \tag{3.1.13}$$

to the open loop function $G(s)$ where τ_d is the delay time. In Fig. 3.1.3 one can see that with a delay the frequency where the phase is inverted is independent of the gain K, and the gain margin is reduced with increasing gain. Thus the time delay in the system limits the gain and the bandwidth of any controller which is able to achieve a stable lock.

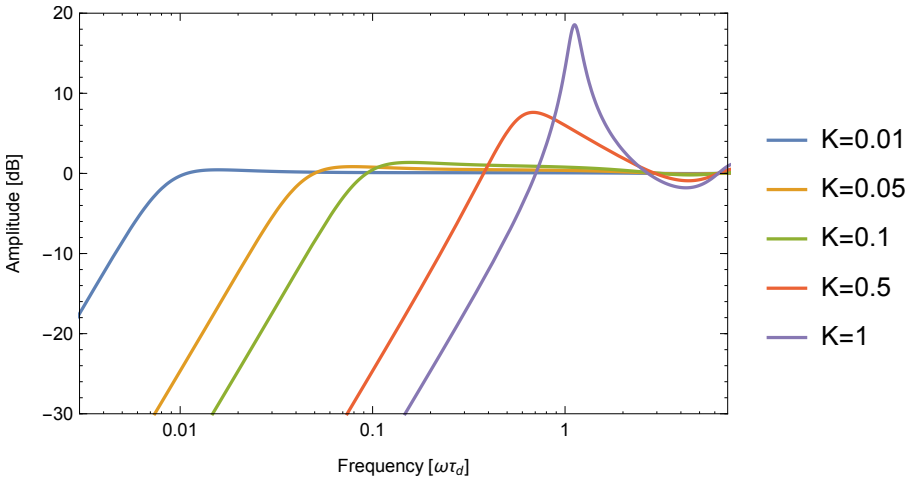

Figure 3.1.5: Frequency response of error function for different values of gain with fixed delay. For large gain values the error function peaks around K.

3.1.4 Servo Bumps

The system transfer function is larger than 0 dB around the gain frequency K. This feature becomes more pronounced for systems with low damping and high gain values. As the stability margin becomes small for high gain values the peak increases because

$$\mathrm{Max}_\omega[|E(i\omega)|] = \frac{1}{\mathrm{Min}_\omega[|1+G(i\omega)|]} = \frac{1}{g_s}. \tag{3.1.14}$$

The system transfer function will amplify noise of the phase detector around this frequency.
Similarly if the error response function is larger than 0 dB at any frequency, phase noise of the oscillator at that frequency is amplified instead of suppressed. This can happen for underdamped systems with small ζ, but also occurs when the gain enters a region comparable with $1/\tau_d$.
Further as the phase locked loop can only compensate for oscillator noise with frequencies lower than the gain K, at higher frequencies the phase noise of the oscillator is not suppressed, and the lineshape of the locked oscillator matches the free running oscillator.
This phase noise can lead to side bands in the spectrum of the oscillator. Considering the effect of phase noise at a single frequency Ω with modulation strength β on an oscillator with a center frequency ω

$$E = E_0 e^{i(\omega t + \beta \sin(\Omega t))} = E_0 e^{i\omega t} \sum_{n=-\infty}^{\infty} J_n(\beta) e^{in\Omega t} \tag{3.1.15}$$

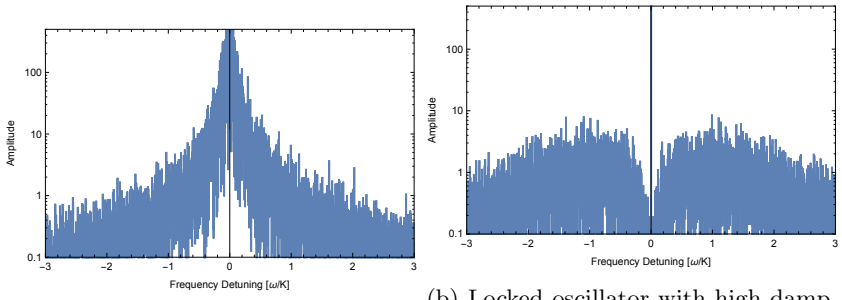

(a) Free running oscillator

(b) Locked oscillator with high damping

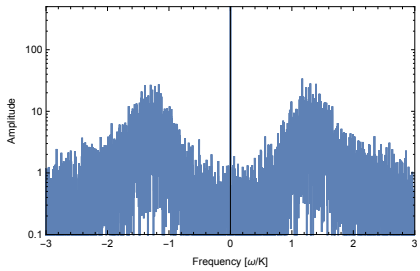

(c) Locked oscillator with low damping

Figure 3.1.6: Simulated spectra of an oscillator with frequency detuning normalized to the gain. For high damping the spectrum corresponds to the free running spectrum for high frequency detunings. For lower damping the servo bumps become stronger.

where the second expression contains an identity using Bessel functions. We can expand in $\beta \ll 1$ and get

$$E \approx E_0(e^{i\omega t}J_0(\beta) + e^{i(\omega+\Omega)t}J_1(\beta) - e^{i(\omega-\Omega)t}J_1(\beta)). \tag{3.1.16}$$

Thus a phase modulation at a frequency Ω generates sidebands in the output of the oscillator. Taking further terms of the expansion into account, one gets additional weaker components at $\omega \pm n\Omega$.
Together this leads to spectral components peaking around $\omega \pm K$ with ω the center frequency of the oscillator, so called servo bumps (Fig. 3.1.6).
In the lock used in the experimental setup these servo bumps are problematic as when one wants to address the sideband transitions of the trapped ion, the servo bumps simultaneously address the carrier transition. The much higher transition probability of the carrier transition makes the servo bumps a significant problem even though they are much weaker than the center frequency.

3.2 Pound-Drever-Hall Locking Technique

Feedback loops require some reference to which they lock. The reference must be very stable as a laser locked to the reference will copy noise of the reference. One possibility is to use the resonances of a Fabry-Pérot cavity.

3.2.1 Cavity Reflection and Transmission

To calculate the transmission and reflection of a cavity one can consider monochromatic light incident on a pair of mirrors with coefficients of reflection r and transmission t. The electric field of the incident light can be written as

$$E_i = E_0 e^{i\omega t} \tag{3.2.1}$$

The amplitude of the electric field that is directly reflected is

$$E_{r0} = E_i r \tag{3.2.2}$$

More light is reflected after undergoing multiple reflections inside the cavity, from this we get contributions

$$E_{r1} = E_i t^2 r e^{i\delta} \tag{3.2.3}$$

$$E_{r2} = E_i t^2 r^3 e^{i2\delta} \tag{3.2.4}$$

$$E_{rn} = E_i t^2 r^{2n-1} e^{in\delta} \tag{3.2.5}$$

where δ is the phase shift acquired by one pass of the cavity. All these contributions can be summed up to

$$E_r = E_i(r + rt^2 e^{i\delta}(1 + r'^2 e^{i\delta} + ... + r'^2 n e^{in\delta})) \tag{3.2.6}$$

As $r < 1$ the series converges and can be written as

$$E_r = E_i(r + rt^2 e^{i\delta}\frac{1}{1 - r^2 e^{i\delta}}) \tag{3.2.7}$$

With zero absorption the coefficients of transmission and absorption are related by $t^2 + r^2 = 1$, simplifying the result to

$$E_r = E_i(\frac{r(1 - e^{i\delta})}{1 - r^2 e^{i\delta}}) \tag{3.2.8}$$

The intensity of the reflected light is then

$$I_r = \frac{|E_r|^2}{2} = I_i \frac{2r^2(1 - \cos\delta)}{(1 + r^4) - 2r^2\cos\delta} \tag{3.2.9}$$

By introducing the coefficient of finesse

$$F = (\frac{2r}{1 - r^2})^2 \tag{3.2.10}$$

the expression can be further simplified to

$$I_r = I_i \frac{F \sin^2(\delta/2)}{1 + F \sin^2(\delta/2)} \tag{3.2.11}$$

The expressions for the intensity are periodic in the phase difference, leading to the concept of the free spectral range (FSR), the frequency difference between two adjacent minima in reflection. The FSR is given by

$$\Delta\nu_{fsr} = \frac{c}{2L} \tag{3.2.12}$$

where c is the speed of light and L the length of the cavity.
The FWHM of the dips in reflection can be calculated as

$$\delta\nu = \frac{c}{\pi L} \arcsin \frac{1}{\sqrt{F}} \approx \frac{c}{\pi L \sqrt{F}} \tag{3.2.13}$$

A further quantity of interest is the Finesse $\mathcal{F}$ [15] which is defined as ratio of the free spectral range and the FWHM

$$\mathcal{F} = \frac{\Delta\nu_{fsr}}{\delta\nu} = \frac{\pi\sqrt{F}}{2} \tag{3.2.14}$$

With the free spectral range the reflection coefficient can now be written as function of the frequency of the light

$$F(\omega) = \frac{E_r}{E_i} = \frac{r(\exp(i\frac{\omega}{\Delta\nu_{fsr}}) - 1)}{1 - r^2 \exp(i\frac{\omega}{\Delta\nu_{fsr}})} \tag{3.2.15}$$

3.2.2 Cavity Filtering

When the laser frequency is locked to the resonance frequency of the cavity, light can pass through the cavity. The intensity of the transmitted beam can similarly be derived as the reflected intensity, or calculated from the assumption of zero absorption,

$$I_t = I_i - I_r = I_i \frac{1}{1 + F \sin^2(\delta/2)} \tag{3.2.16}$$

The transmission is strongly suppressed when the laser frequency is off resonant from a cavity resonance. This feature is used here to clean the spectrum of the 729 nm laser light. Fig. 3.2.2 shows the calculated transmission of a cavity with the parameters of the high finesse cavity used in the experiment. At 1.5 MHz where the servo bumps are located, the transmission is suppressed by 5 orders of magnitude.

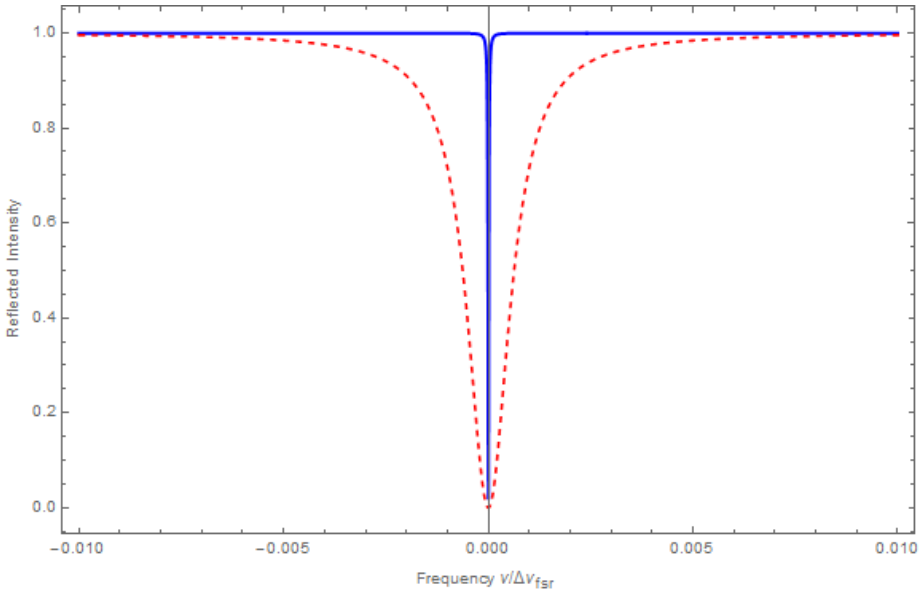

Figure 3.2.1: Calculated intensity of reflected light for a cavity with values of finesse 1000 (red) and 270000 (blue) respectively.

3.2.3 Phase Modulation

A very simple locking scheme measures the reflected intensity from the cavity (Fig. 3.2.1). The laser is then locked to a set intensity value. This scheme suffers from the drawback that the lock cannot distinguish between frequency and intensity drifts of the laser.
A lock to the minimum of the transmission signal is preferable, as it decouples intensity and frequency, however the signal is symmetric around its minimum, making it impossible to know in which direction to apply a correction.
The Pound Drever Hall [16] scheme (Fig. 3.2.3) solves this by phase modulating the laser signal, generating sidebands. This can be done using an electro-optic modulator (EOM). The electric field of a laser with frequency ω with such a modulation is given by

$$E_i = E_0 e^{i(\omega t + \beta \sin \Omega t)} \tag{3.2.17}$$

This expression can be expanded using Bessel functions[17], keeping only terms up to first order assuming the modulation parameter β is small

$$E_i \approx E_0[J_0(\beta)e^{i\omega t} + J_1(\beta)e^{i(\omega+\Omega)t} - J_1(\beta)e^{i(\omega-\Omega)t}] \tag{3.2.18}$$

The reflected electric field can be calculated by treating each frequency component separately.

$$E_r \approx E_0[F(\omega)J_0(\beta)e^{i\omega t} + F(\omega+\Omega)J_1(\beta)e^{i(\omega+\Omega)t} - F(\omega-\Omega)J_1(\beta)e^{i(\omega-\Omega)t}] \tag{3.2.19}$$

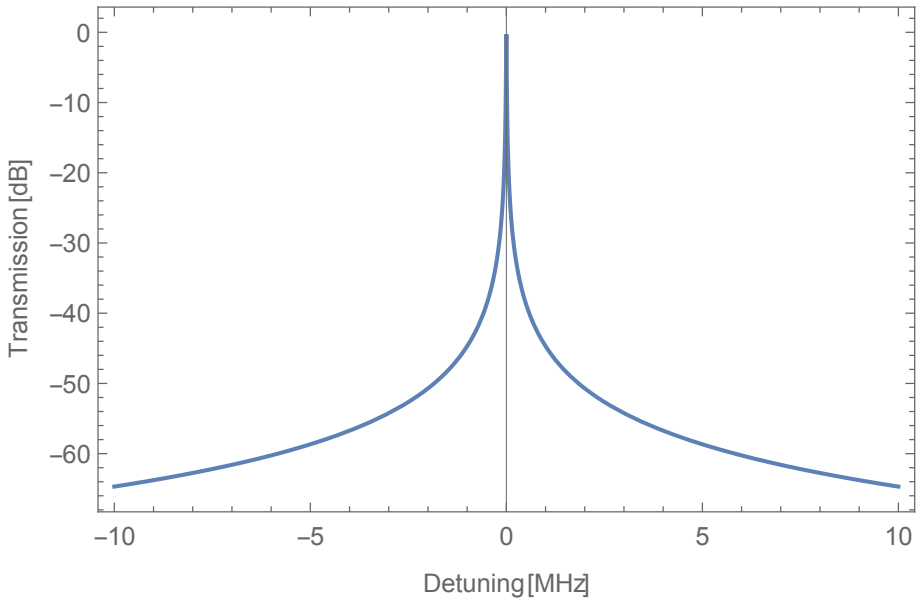

Figure 3.2.2: The transmission of a cavity with a free spectral range of 2.14 GHz and a Finesse of 270000 plotted on a logarithmic scale.

The intensity of the reflected field is again given by

$$\begin{aligned} I_r = \frac{|E_r|^2}{2} = |E_0|^2(&|F(\omega)J_0(\beta)|^2 + |F(\omega+\Omega)J_1(\beta)|^2 + |F(\omega-\Omega)J_1(\beta)|^2 \\ &+ 2J_1(\beta)J_0(\beta)\{ \\ &\Re(F(\omega)F(\omega+\Omega)^* - F(\omega)^*F(\omega-\Omega))\cos(\Omega t) \\ &\Im(F(\omega)F(\omega+\Omega)^* - F(\omega)^*F(\omega-\Omega))\sin(\Omega t) \\ &+ (2\Omega \text{ terms})\}) \end{aligned} \quad (3.2.20)$$

In this expression we are only interested in the terms varying with Ω. They can be extracted by mixing the photodiode signal with a reference signal at frequency Ω. We now assume that the carrier is near resonance and the modulation frequency is large enough so the sidebands are not, then the sidebands are totally reflected ($F(\omega \pm \Omega) \approx 1$). In this case the cosine term vanishes, and only the sine term remains as $F(\omega) - F(\omega)^*$ is purely imaginary.
The shape of the error signal is shown in Fig. 3.2.4. The steep slope around zero allows very sensitive locking, and the position of the sidebands determines the capture range. For increasing modulation frequencies the amplitude of the error signal between the side bands and the center line goes to zero, thus limiting the maximum possible capture range in practice.
When extracting the error signal by mixing it with a reference from a local

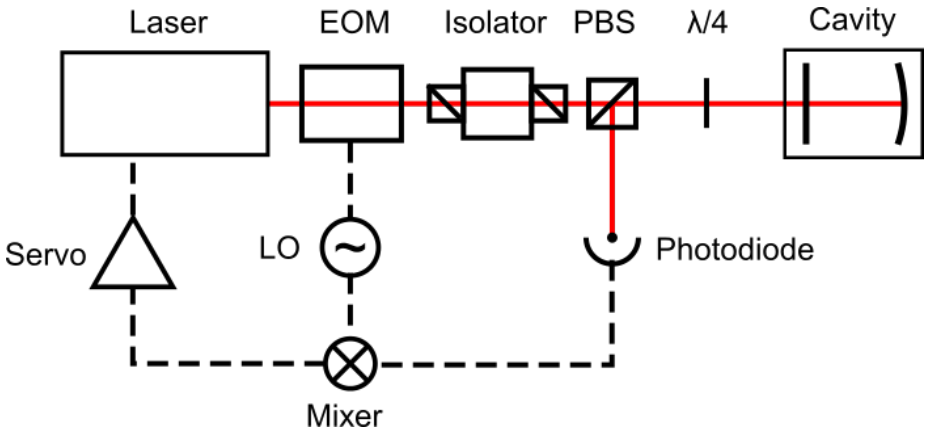

Figure 3.2.3: Optical Setup of a PDH lock. The electrooptic modulator adds sidebands to the spectrum which produces an antisymmetric error signal on reflection, which is then used to feed back to the laser. The Faraday isolator prevents the reflection from the cavity returning to the laser.

oscillator we get two components

$$\sin(\Omega t)\sin(\Omega' t + \varphi) = \frac{1}{2}\{\cos((\Omega - \Omega')t - \varphi) - \cos((\Omega + \Omega')t + \varphi)\} \quad (3.2.21)$$

The second term can be neglected as it is much faster than the controller, leaving only a DC signal for $\Omega = \Omega'$, however this signal vanishes for $\varphi = \frac{\pi}{2}$. This phase has to be matched to get a good error signal (Fig. 3.2.5), which can be done by adding a delay line either between local oscillator and the EOM or the photodiode and the mixer.

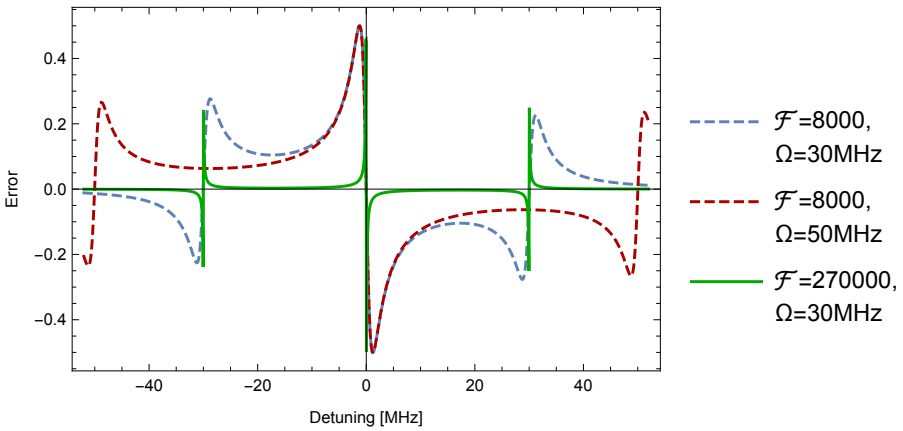

Figure 3.2.4: PDH error signal for different values of finesse and modulation frequency.

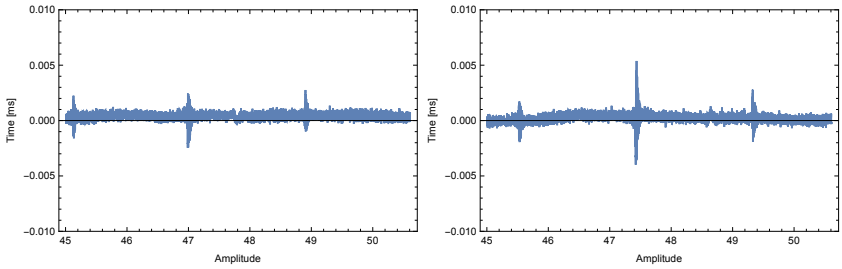

(a) not phase matched (b) phase matched

Figure 3.2.5: Measured PDH error signal with different delay lines.

3.3 Phase Lock

The 729 nm laser used for $^{40}Ca^{+}$ ion control was previously stabilized by locking it to a high finesse cavity by an analog PID controller[1] via a PDH locking scheme (See Fig. .0.1). The laser system[2] has two ports, a diode port which provides the light necessary for the lock to the cavity and a main port where the output of the diode has been amplified by a tapered amplifier (TA). This also amplifies the servo bumps present in the emission spectrum due to the control scheme.
To be able to work with the cavity without shutting down the ion trap experiments dependent on 729 nm light the laser was beat locked to a second 729 nm laser which is stabilized by its own high finesse cavity via PDH technique (Fig. .0.2). For this light from the master and light from the diode port of the

[1]Toptica FALC-110 fast analog control unit
[2]Toptica TA pro

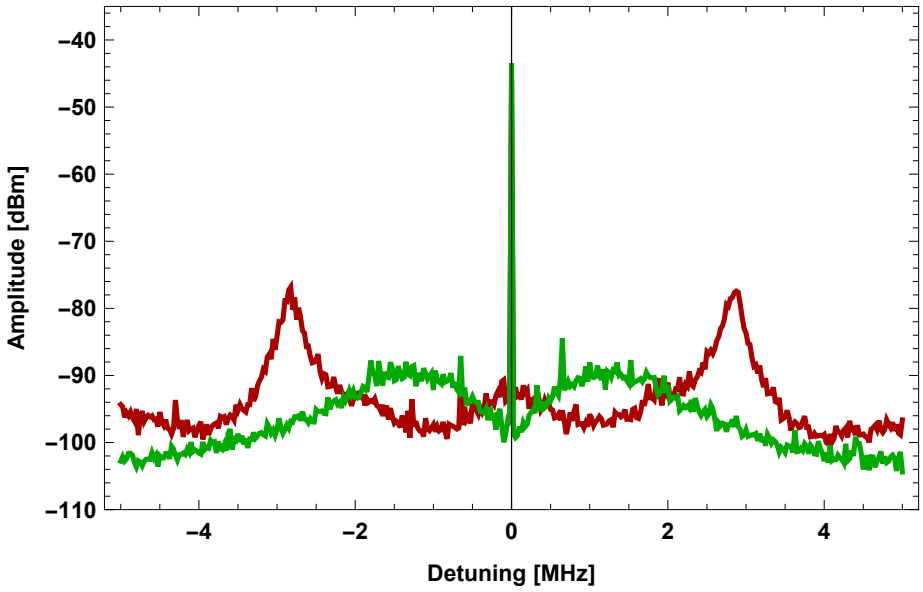

Figure 3.3.1: Beat note between the two 729 lasers with high (red) respectively low (green) gain of the controller. The servo bumps are ≈ 40 dB lower than the center peak for low gain, the reduction is ≈ 30 dB for high gain. This trace was taken with the first laser locked to a high finesse cavity and the second phase locked to the first laser.

slave laser were combined on a beam splitter (Fig. 3.3.2). The resulting beat note was measured on a fast photodiode[3] (Fig. 3.3.1). The beat note was mixed down with a 690 MHz RF source[4]. The slave laser was then locked to this error signal by the same FALC-110 control unit.

To set up the beat note first one beam was aligned with the photodiode, which is placed at the focal point of a lens to maximize the signal. The second beam then can be overlapped with the first by walking the two adjustment mirrors. The photodiode is monitored with a spectrum analyzer. Once a beat note is measured, it can be optimized by walking the second beam again and properly centering the combined beam onto the photodiode.

Each signal has to be checked if it is truly an interference signal of the two beams. As the RF source used to generate the LO signal produces a pickup signal at the exact frequency of the beat note, 40 dB of amplification were used to ensure the signal was larger than the pickup, as well as generate a sufficiently large error signal for the controller.

The parameters of the FALC-110 analog control unit had to be adjusted for the new lock. The FALC-110 has two output channels, a fast branch acting on the current of the laser and a slow branch acting on a piezo controlling one of

[3]Home built design using a Hamamatsu S5973-02 Si PIN diode.
[4]Trinity Power Incorporated RF Signal Generator Version 4.0

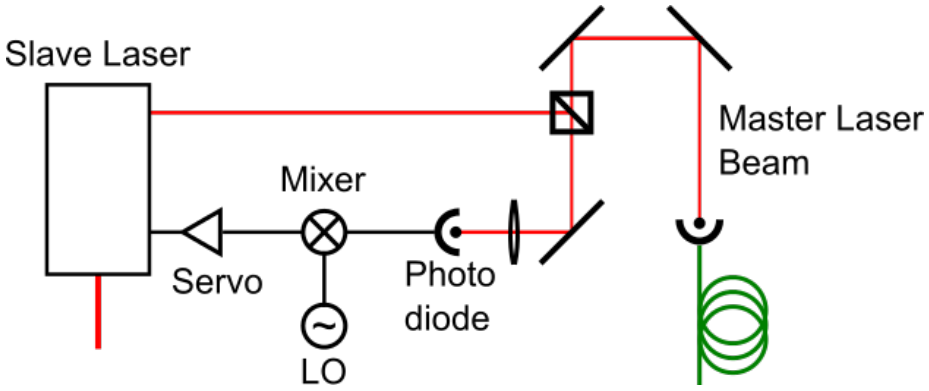

Figure 3.3.2: Setup of the beat lock. Light from the master and the slave laser are overlapped and their beat note is measured on a fast photodiode. The signal is then mixed down with a local oscillator (LO) and then fed back to the slave laser.

the laser cavity mirrors. The parameters were tuned by monitoring the error signal and the outputs of both branches on an oscilloscope and the beat note on a spectrum analyzer. The offset of the fast branch was adjusted so the error signal was centered around zero. The fast branch has a fast differentiator, a fast integrator, a slow integrator and an extra slow integrator (XSLI). The fast differentiator, the fast and slow integrator were set as high as possible without unlocking the laser. The XSLI was left turned off.
The unlimited integrator (ULI) of the slow branch was tuned once the fast branch was stable. The offset was tuned so that the output which was monitored on an oscilloscope remained zero after the ULI was turned on.

Chapter 4

Filtering the spectrum

4.1 Cavity Incoupling

The cavity used as a filter is a high finesse optical reference cavity that was designed by R.Leibrandt et al. [18] at the National Institute of Standards and Technology (NIST) and then fabricated by Advanced Thin Films.
The finesse of the cavity was determined via ring-down measurement to be around 270000 [19]. The cavity has a free spectral range of 3.14 GHz, resulting in a linewidth of 11.7 kHz.
The light from the slave laser was locked to the cavity by the PDH technique, however instead of directly controlling the laser an acousto-optic modulator (AOM) was used to control the laser frequency (Fig. 4.1.1). This is only possible as it is already known that the laser frequency is close to a resonance frequency of the cavity, as the modulation range of the AOM is much smaller than the free spectral range of the cavity.

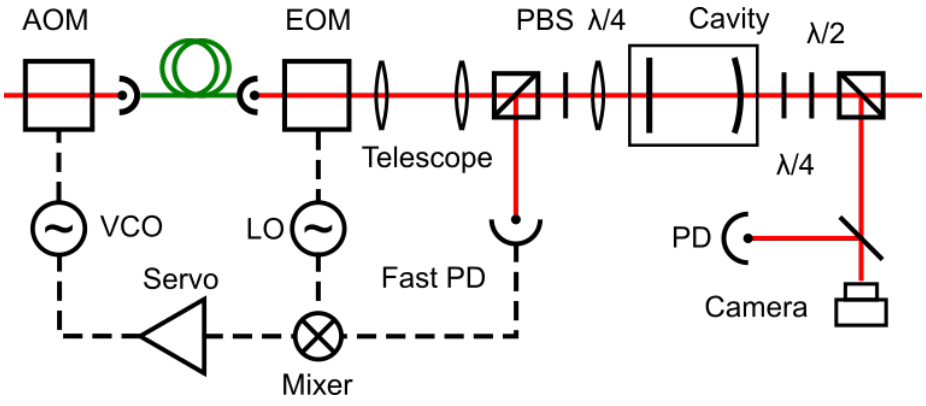

Figure 4.1.1: Pound Drever Hall scheme for locking a laser using an acousto-optic modulator. An EVIL lockbox[1] was used as servo.

4.1.1 Optical Setup

The polarization of the light going to the cavity is changed from linear to circular by using a $\frac{\lambda}{4}$ waveplate. This has the advantage that σ_+ polarized light is changed to σ_- polarized light on reflection from the cavity mirror. When passing the $\frac{\lambda}{4}$ waveplate again, the light is perpendicularly polarized to the incoming beam, and thus can be separated from the incoming beam using a polarizing beam splitter cube. The light was then focused onto a fast photodiode[2].
An optical isolator was placed before the polarizing beam splitter to prevent etaloning between the cavity mirrors and any other optical element. The beam was matched to the cavity by using a telescope and a focusing lens. The two mirrors define a single Gaussian beam whose wavefronts matches the surface of both mirrors. The required waist size at the planar mirror was calculated as $W_0 = 369\,\mu$m. As the beam coming out of the fiber is well collimated the waist size is first expanded with a telescope so it matches the required spatial mode on the focusing lens which is placed such that its focal point coincides with the planar mirror of the cavity.
The cavity transmission was monitored on a slow photodiode and a camera. The camera proved useful to identify the Gaussian TEM_{00} mode and the photodiode was used to maximize the transmission. A $\frac{\lambda}{4}$ wave plate was first used to restore linear polarization, then a $\frac{\lambda}{2}$ wave plate and a polarizing beam splitter were used to control the amount of light sent to either the monitoring setup or the diode injection setup respectively.

4.1.2 Incoupling Procedure

To find the desired TEM_{00} mode the laser frequency was first scanned. A viewcard with a hole was used to search for the back reflection off the cavity mirror, which was overlapped with the incoming beam. Not all reflections observed were from the cavity mirror, the windows of the vacuum housing produced reflections as well.
Once the beams are well overlapped, the camera was used to search for any modes in the transmitted light. As the frequency of the light is scanned, the modes are much weaker than the scattered light that is also visible on the far side of the cavity. The frequency of the scan should be low to make the modes more visible. Once a mode has been observed, the beam can be walked to the TEM_{00} mode. At this point a useful error signal can already be recorded, and the frequency of the light can be locked to the cavity.
The slow photodiode behind the cavity is then used to monitor the transmission, which is optimized by iteratively readjusting the telescope length, the telescope lens positions, the focusing lens position and walking the alignment mirrors.

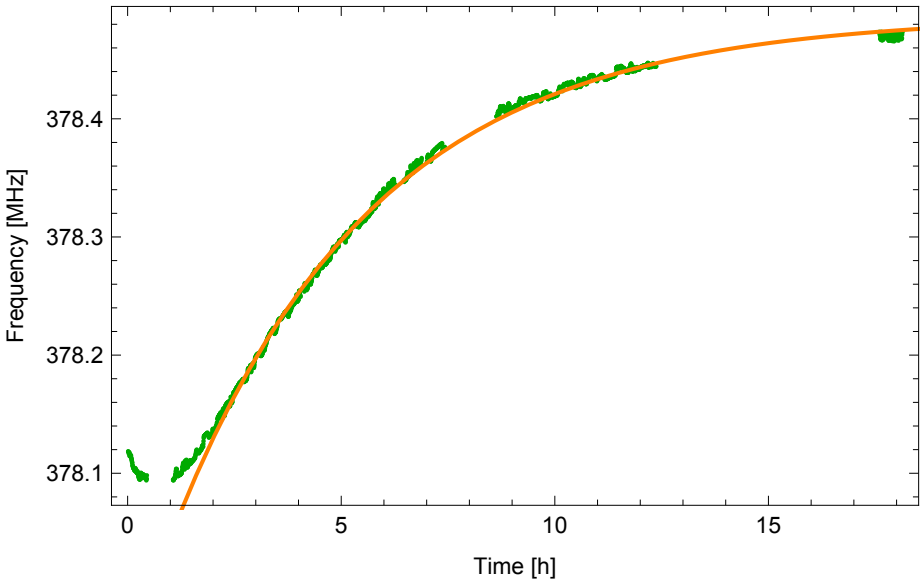

Figure 4.1.2: Frequency shift of cavity after changing temperature set point. The missing regions correspond to times when one of the lasers was not locked. At about 1h the frequency drift changes sign as the cavity passes the zero-crossing temperature. An exponential fit gives a timescale of $\approx 5h$

4.1.3 Zero-Crossing Temperature

The resonance frequency of a cavity depends on the temperature of the cavity. The optimal temperature to operate a cavity at is the so called zero-crossing temperature where the derivative of the resonance frequency with respect to temperature vanishes $\frac{d\nu}{dT} = 0$, as the contributions from distortions of the mirror interfaces and the cavity length cancel out [22]. As a result the resonance frequency of the cavity becomes insensitive to first order to temperature fluctuations.
Having two lasers locked to high finesse cavities allows to accurately determine the zero-crossing temperature by monitoring the beat note between the two lasers as the temperature of one cavity is changed. After changing the temperature the cavity needs time until it thermalizes (Fig. 4.1.2).
The measured resonance frequencies were plotted as function of temperature and fitted with a parabola (Fig. 4.1.3). The minimum of the fitted parabola gives a zero-crossing temperature of $-4.4 \pm 0.1\,^{\circ}\mathrm{C}$. This result is much lower than the zero-crossing temperature of $1.4 \pm 1\,^{\circ}\mathrm{C}$ determined by the manufacturer via a speed of sound measurement [23].
The frequency drift of the beat note of the two lasers was monitored over time

[1] Home-built FPGA based PID controller. See [20]
[2] KPD 110 fast photodiode (up to 200 MHz) Designed by B. Keitch [21]

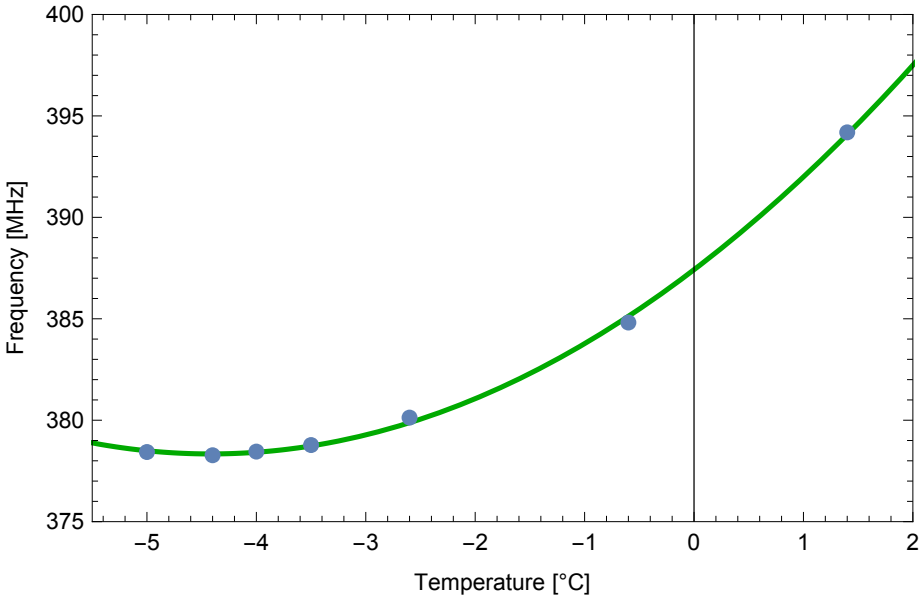

Figure 4.1.3: Frequency shift of the cavity dependent on temperature. The frequency scale is relative to the second 729 nm laser. A minimum is reached at $-4.4 \pm 0.1\,^{\circ}\mathrm{C}$

.

(Fig. 4.1.4). The steepest slope observed was 0.37 Hz/s. This value is comparable to previous measurements with the cavity at a temperature of 1.4 °C. The limiting factor is likely noise on the fiber leading from the cavity to the beat note.

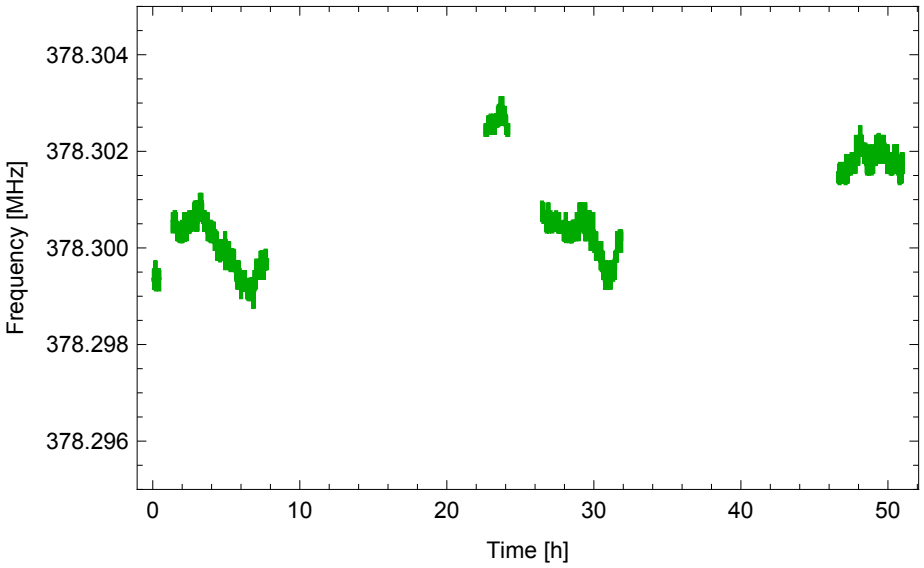

Figure 4.1.4: Frequency drift of the cavity at zero-crossing temperature of $-4.4 \pm 0.1\,^{\circ}\mathrm{C}$

4.2 Diode Injection

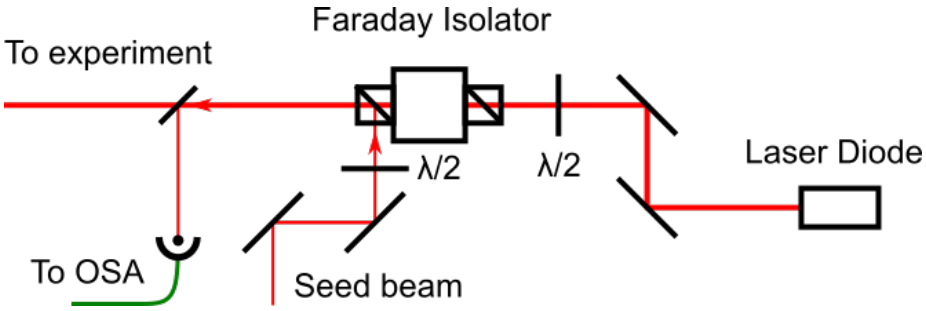

Figure 4.2.1: A diode is injected by sending a seed beam through the side port of a Faraday Isolator.

4.2.1 Experimental Setup

The light transmitted through the cavity is amplified by injecting a laser diode. For this the seed beam from the cavity is sent through the side port of a Faraday isolator (Fig. 4.2.1). The Faraday isolator rotates the polarization of the beam by 45° in the same directions for the incoming seed beam and the outgoing diode light. A beam that is reflected back into the isolator thus acquires a total

shift of 90°. This results in keeping the emission from the diode from coupling into the cavity. The seed beam forces the laser diode to emit light with the same spectrum as the injected light. A first wave plate is used to match the seed beam polarization to the Faraday isolator and a second plate to match the polarization between diode and isolator.
Two diodes have been tested in the diode injection setup, a laser diode with anti reflective coating[3] and a diode without anti reflective coating[4]. Both diodes were tested mounted in a collimation tube[5] in the same custom mount [24]. Temperature and current control was provided by a Vescent Photonics D2-105 controller [25].

4.2.2 Alignment

The Faraday Isolator[6] was first aligned with the output beam of the laser diode. The collimation tube has a lens[7] mounted in front of the diode. The lens position had to be adjusted with a spanner wrench to collimate the diode output. The waveplate between isolator and diode was adjusted to maximize transmission through the isolator. For high diode currents, some light can be seen at the side port of the isolator. The seed beam is then overlapped with this beam using two alignment mirrors.
The output beam was coupled into a fiber and sent to an optical spectrum analyzer for monitoring the output of the diode.

4.2.3 Coated Diode

For the coated diode the injection peak was visible for all tested temperatures and low currents. At high currents the injected power was insufficient to suppress the natural mode, and both the natural and the injected mode were present in the spectrum.
For certain combinations of current and temperature the output reached a local maximum. This is due to the two surfaces of the laser diode forming a resonator. This resonator is very lossy due to the anti reflective coating of the diode. Both current and temperature affect the length and refractive index of this cavity, leading to a shift in resonance. The maxima appear when a resonance matches the laser frequency. The maxima lie on approximately straight lines and are independent of the power of the injected beam (Fig. 4.2.2).
For low current the injection of the diode increases the power emitted from the diode. The increase depends on the injected power due to the injected light lowering the lasing threshold of the diode (Fig. 4.2.3).

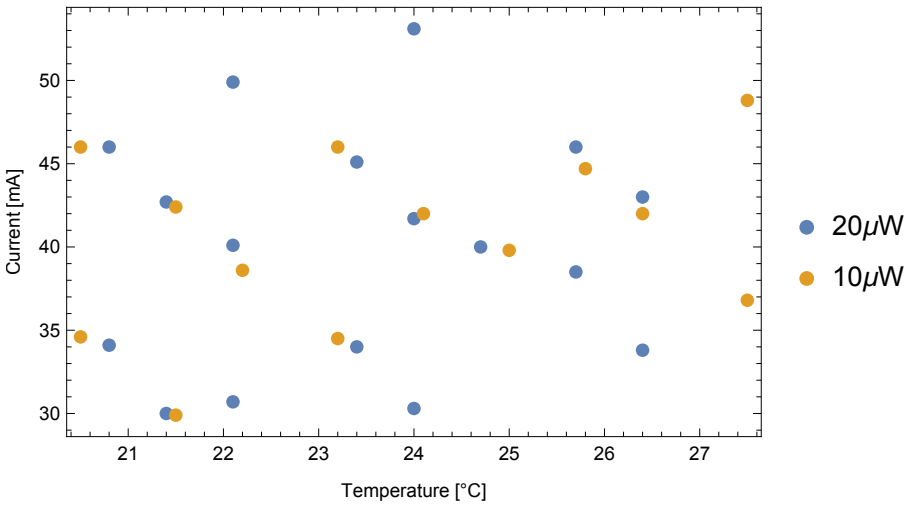

Figure 4.2.2: Points of clean injection for coated diode plotted vs temperature and current. The points lie on parallel lines. The lines do not depend on injected power.

4.2.4 Uncoated Diode

The coated diode was replaced with an uncoated one. Realignment of the setup was required after the change of diode. The uncoated diode was much more sensitive to finding maxima. These maxima called points of clean injection could be found over a wide range of temperatures and over the entire range of currents (Fig. 4.2.4). However unlike the coated diode other modes appeared in the spectrum in the current range between these points of clean injection. For a given temperature the injection peak was only visible in the OSA spectrum over a small current range of $\approx 1 - 2\,\mathrm{mA}$. The range for clean injection where the natural emission was fully suppressed was only $\approx 0.1\,\mathrm{mA}$. This behavior is expected as the uncoated diode surfaces form a better resonator compared to the coated diode. When the injected beam does not match the resonator, the injected power circulating in it is very low, and the natural mode dominates.

[3] Toptica #LD-0730-0040-AR-2
[4] Thorlabs HL7302MG
[5] Thorlabs LT230P-B
[6] Qioptiq LINOS Faraday Isolator FI-730-5SV
[7] A390TM-B

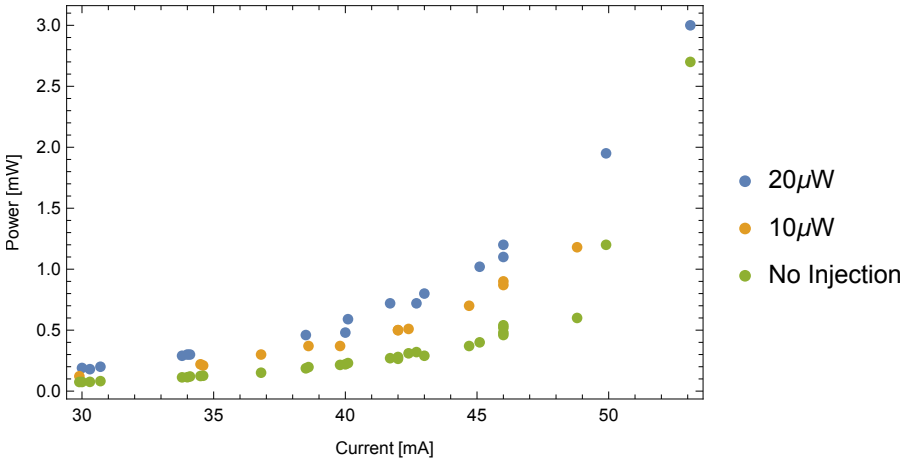

Figure 4.2.3: Diode output power for different currents at 10 μW and 20 μW. Data points were taken at points of clean injection. An increase in output power is visible at all currents. The difference decreases as the diode passes its free running lasing threshold.

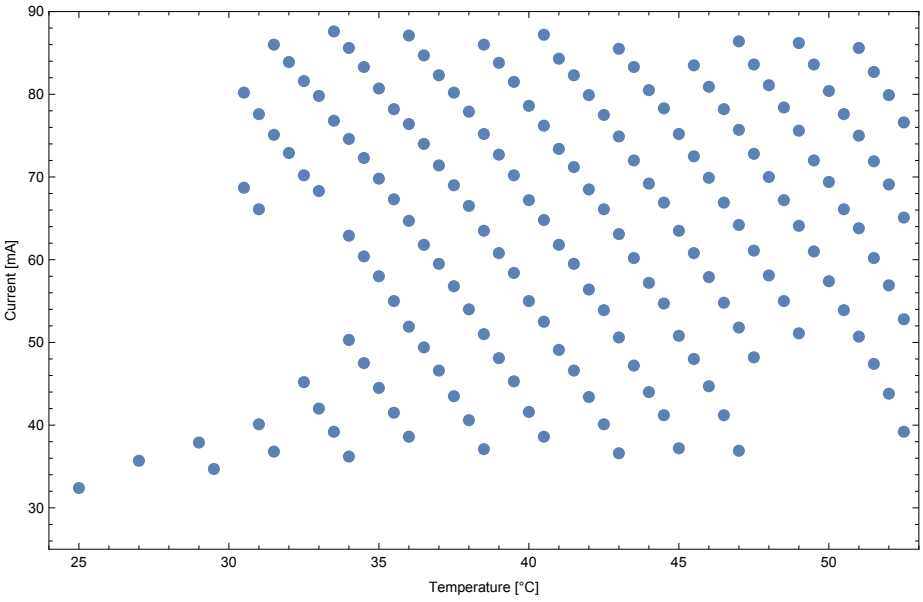

Figure 4.2.4: Points of clean injection for uncoated diode at 40μW injection power plotted vs temperature and current. The points of clean injection lie on straight, equally spaced lines.

4.2.5 Mininmum injection power

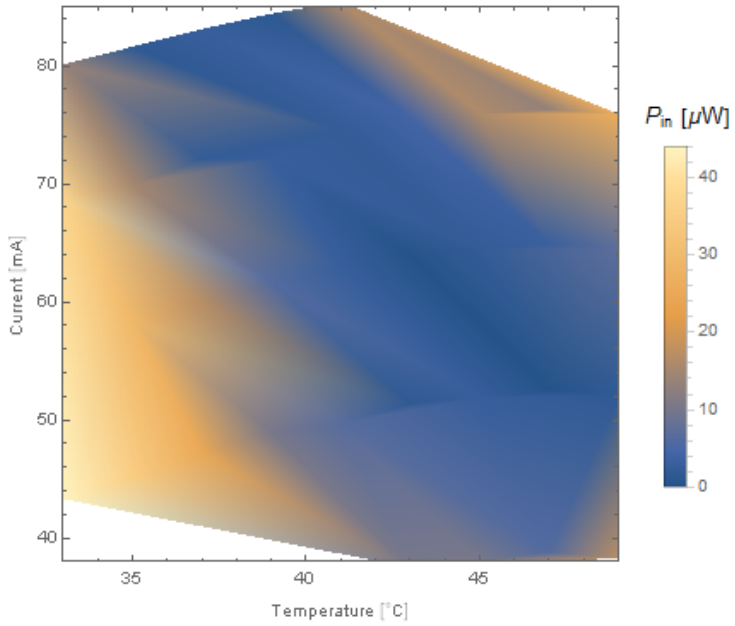

Figure 4.2.5: Minimum power required for clean injection using uncoated diode. Measurement points were taken at points of clean injection

For the uncoated diode the minimal injection power was determined by reducing the injection power until the spectrum observed on the OSA was no longer clean. The injection power was then increased again until clean injection was restored.
The formula for the minimum injection power[26] required for a clean injection is given by

$$\frac{I_0}{I_{out}} = \frac{\sqrt{R_1R_2}(1+\sqrt{R_1R_2}^{2-2\alpha_n/\alpha_i} - 2\sqrt{R_1R_2}^{1-\alpha_n/\alpha_i}\cos\delta)}{(1-R_1)(1-R_2)}, \tag{4.2.1}$$

where R_1, R_2 are the reflectivities of the surfaces, δ is the phase mismatch of the injected light to the cavity and α_i is the gain coefficients at the injection frequency and α_n is the gain coefficient at the natural frequency (See Fig. 4.2.6). For perfectly matched light $\delta = 0$ the minimum injection power is given by

$$\frac{I_0}{I_{out}} = \frac{\sqrt{R_1R_2}(1-\sqrt{R_1R_2}^{1-\alpha_n/\alpha_i})^2}{(1-R_1)(1-R_2)}, \tag{4.2.2}$$

If the gain coefficients are equal, the required injection power drops to zero. This suggests that the inability to inject the coated diode at high currents is a result of the gain at the injected frequency being much lower than the gain at

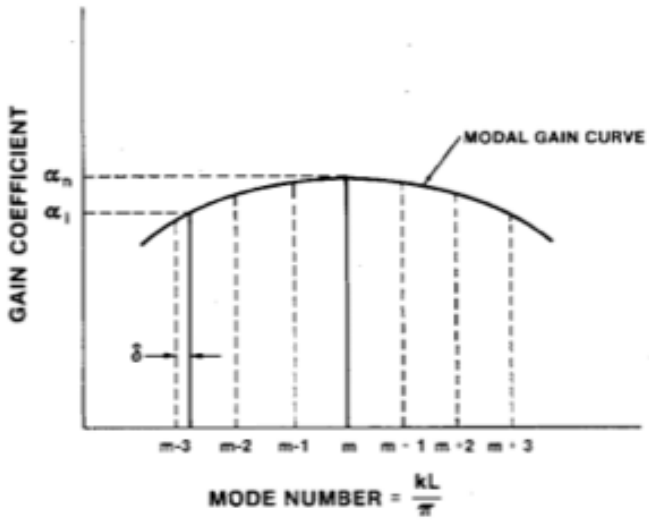

Figure 4.2.6: The natural mode a diode emits from will be the resonator modes with the highest gain coefficient α_n. An injected mode will both have a gain coefficient α_i lower than the natural gain coefficient and a phase mismatch δ to the nearest resonator mode. From [26]

the natural frequency, and does not result from the anti-reflective coating.
In Fig. 4.2.5 at the lower end of the temperature range the required injection power decreases for increased current and thus increased output power at lower temperatures. This is due to the natural emission wavelength being shifted closer to the injected wavelength, thus decreasing the required injection power.

4.2.6 Long term stability

The long term stability of the diode injection was monitored by reading out the OSA output with a data-logger[8]. After the injection was initially established, the diode thermalized and required readjustment after $\approx 20-30$ minutes. Once the diode had settled the injection remained stable over multiple days.
The laser unlocking leads to a loss of the transmission and thus to a loss of the injection, however relocking the laser immediately restored the diode injection. Similarly the diode could be switched off, once turned on and left to thermalize for 30 minutes injection was restored without any change to the current.

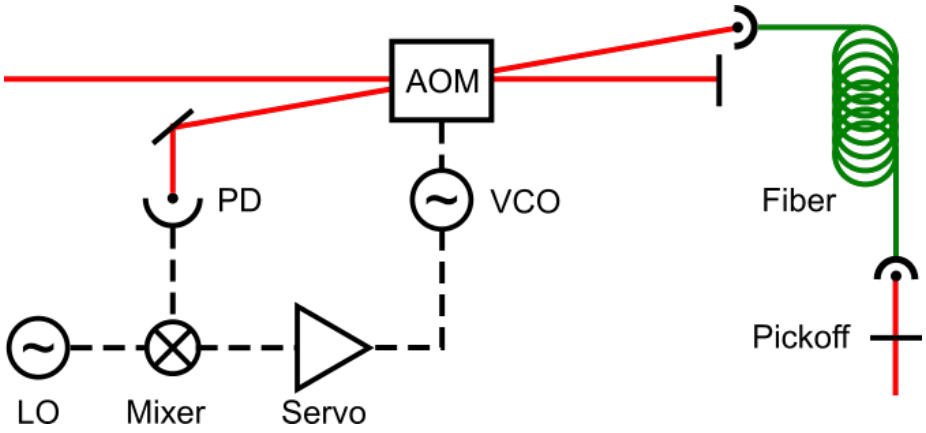

Figure 4.3.1: Setup for fiber noise cancellation. The beat signal of the promptly reflected light and the light back-reflected through the fiber is used as error signal to apply a cancelling phase shift with the AOM. The deflection angle of the beam at the AOM is exaggerated for legibility.

4.3 Fiber Noise Cancellation

Fibers are used to transfer light between the optical tables. They have the advantage of allowing to separate the laser system from the ion trap and decoupling the alignment of different parts of the optical setup.
Fibers can induce phase shifts due to small differences in temperature and pressure in the laboratory as well as mechanical stress on the fiber, broadening the linewidth of the laser [28]. This effect increases with the length of the fiber, thus to preserve the narrow linewidth a scheme to cancel the phase noise of the fiber is necessary. The idea is hereby to apply a negative phase shift to the light. The setup is based on a scheme from the Ion Storage Group at NIST[29] and was used in the group before [11] [30].
Part of the light passing though the fiber is back reflected back into the fiber. The back reflected light acquires the phase shift of the fiber twice. Some light is back-reflected without passing through the fiber. These two beams form a beat note at twice the operating frequency of the AOM, and the phase of the beat note contains twice the phase shift induced by the fiber. The signal is mixed down with a reference and used as error signal for the servo to feed back on the AOM. For the cancellation scheme to work the fluctuations have to be slower than the bandwidth of the cancellation system.

4.3.1 Optical Setup

To set up a fiber noise cancellation setup first the AOM has to be aligned (Fig. 4.3.1). For this the AOM is first placed perpendicular to the laser beam

[8] RedPitaya, for more information see [27]

which is aligned horizontally above the optical table. The AOM is then turned such that the diffracted orders become visible. A focusing lens is placed before the AOM, the maximum possible diffraction efficiency strongly depends on the focal length and position of the lens. A second lens was placed after the AOM to collimate the beam again for coupling it well into the fiber.
The first order diffraction can now be coupled into the fiber, while the zeroth order is back-reflected with a mirror. Properly aligned the zeroth order produces a diffracted beam in the minus first order on returning through the AOM. For fibers with flat connectors at the far end, a back-reflection is already automatically properly aligned, and the two reflections can be overlapped and focused onto a photodiode[9]. For angled connectors a pick-off has to be aligned by first aligning the prompt back-reflection to estimate the position of the reflection. A power meter is placed where the minus first order of the prompt back-reflection at the AOM appears and the prompt reflection is blocked afterwards. The reflection from the pick-off now can be aligned by eye in the horizontal direction, aimed above the collimation lens of the connector. The pick-off is then scanned in the vertical direction until a signal is seen on the power meter. Once a signal is observed it can be optimized in both horizontal and vertical direction.
When both reflections are present the back-reflection from the fiber can be focused onto the photodiode, and the prompt reflection is then overlapped with the first reflection until a beat note is observed. Surfaces of the AOM can also form back-reflections which possibly interfere with the beams and produce a beat note as well. To confirm the beat note, it has to vanish on blocking either beam, and a noise pedestal of noise from the fiber should be present.

4.3.2 Electronic Setup

The AOM frequency now can be locked to cancel this phase shift. For this a EVIL lockbox is used as servo which is connected to a home built POISON board. The board includes both the mixer[10] to generate the error signal for the EVIL and the voltage controlled oscillator (VCO)[11] on which the servo feeds back. A RF synthesizer[12] was used as LO.

4.3.3 Spectrum

The EVIL lockbox has a P, I and D gain that can be adjusted. Without P gain the beat note of the fiber noise cancellation setup is broadened both due to the noise of the fiber and the noise from the VCO used to drive the AOM. At low P gain the center peak becomes narrower as the phase of the VCO is locked to the reference. With increasing P gain the noise close to the center peak is suppressed. At the same time the servo bumps appear in the spectrum. At very high P gain the servo bumps become very large in the spectrum up to the point

[9] Home built design using a Hamamatsu S5973-02 Si PIN diode.
[10] Minicircuits ADE-1L or ADEX-10L
[11] Minicircuits JTOS, model chosen dependent on desired operating frequency
[12] Trinity Power Incorporated RF Signal Generator Version 5.0

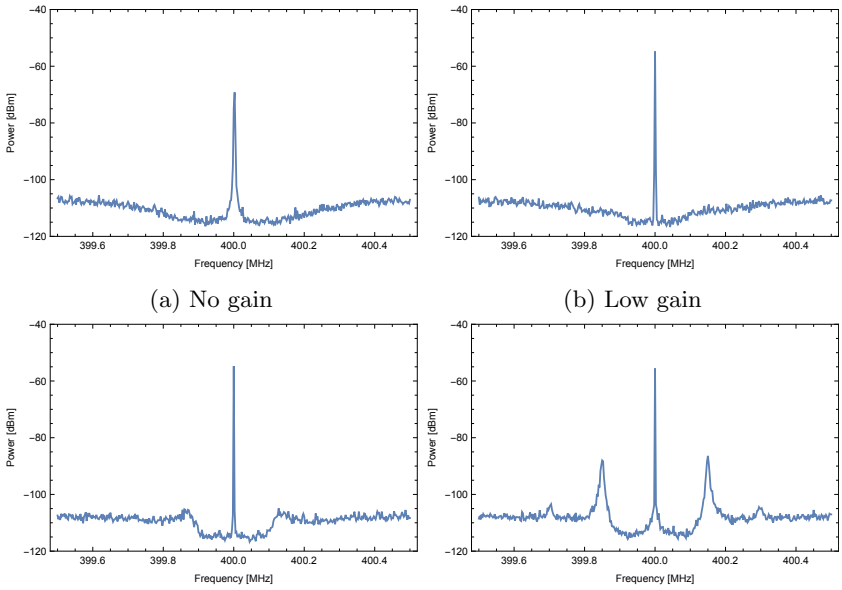

(a) No gain (b) Low gain

(c) Medium gain (d) High gain

Figure 4.3.2: Beat signal of a FNC setup. For higher gain settings servo bumps appear in the spectrum. At very high gain second order servo bumps are visible at twice the controller bandwidth.

where the second servo bumps become visible at twice the frequency.
The I gain is essential initially for the control loop to settle, however once locked, little effect has been observed in the spectrum for different I gain settings. No effect of the D gain on lock stability could be found, and it is left at 0.

4.4 Laser at ion

4.4.1 Laser Spectrum

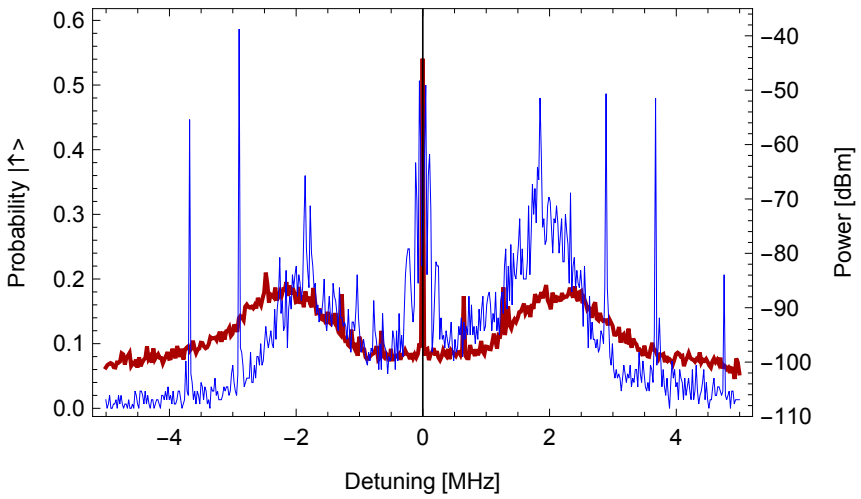

Figure 4.4.1: Spectrum on ion using filtered light. The 729 nm probe pulse duration was set to 50 μs,, corresponding to 10 π times of the carrier. The beat note of the laser light is shown in red.

A single $^{40}Ca^{+}$ ion was trapped and used to measure the spectrum. In the experiment the ion was first prepared in the ground state, then a single laser pulse with a variable detuning was applied. Afterwards the ion state was read out. This procedure measures if any spectral component drives any transition of the ion, either carrier or sideband transition.
A clear improvement is visible in Fig. 4.4.2 compared to Fig. 4.4.1. In the unfiltered spectrum the sidebands are covered by the servo bumps driving the carrier transition. For the filtered light the first and second axial and the first radial mode are clearly visible, while no contributions from the servo bumps driving the carrier transition are visible.
For a π time of 5 μs of the carrier transition a π time of 30 μs is expected for the first sidebands with $\eta = 0.05$ and a thermal state with $\bar{n} = 10$. The servo bumps driving the carrier have a π time of 160 μs assuming they are 30 dB suppressed compared to the line center. This is comparable to the measured spectrum (Fig. 4.4.1) where the measured servo bumps correspond to π times of $\approx 140\,\mu$s.

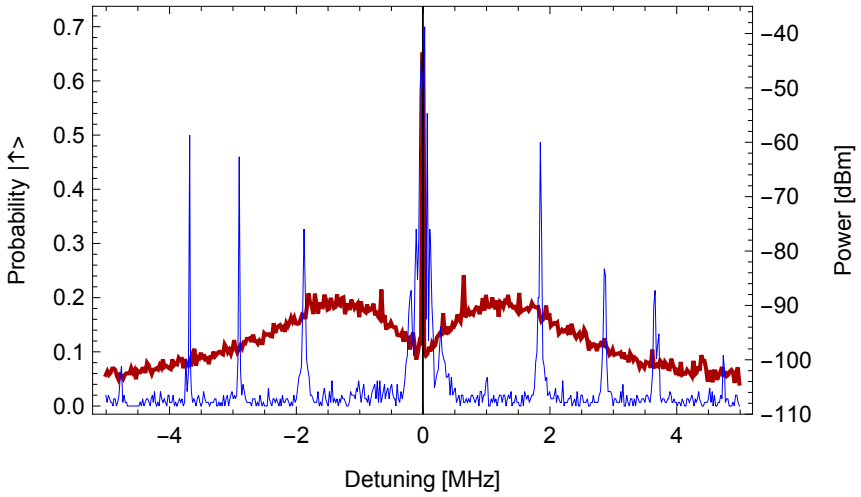

Figure 4.4.2: Spectrum on ion using filtered light. The 729 nm probe pulse duration was set to 50 μs, corresponding to 10 π times of the carrier. The beat note of the laser light is shown in red.

With the cavity suppressing the servo bumps by additional 50 dB the π time increases to 50 ms, and in the spectrum of the ion (Fig. 4.4.2) no servo bumps are visible.

4.4.2 Rabi Oscillations

Rabi oscillations can be measured by applying a laser pulse for a certain duration to the ion and then reading out the state of the ion.
Fig. 4.4.3 shows Rabi oscillations on the blue sideband for unfiltered light. For a high gain of the Servo the contrast of the oscillations decays fast due to strong servo bumps driving the carrier transition. Rabi oscillations on the carrier transitions (Fig. 4.4.4) show a different behaviour with unfiltered light, where the contrast of the oscillations decays fast for low gain settings as the laser linewidth is not narrow enough anymore. Thus with unfiltered light a trade off is necessary between high gain producing servo bumps which result in poor sideband transitions, and low gain leading to poor carrier transitions.
With filtered light the contrast of the Rabi oscillations show no dependence on the gain setting (Fig. 4.4.5). The contrast of the oscillations decays slower with the filtered light, even with the lowest gain setting only a value of $\tau = 1$ ms

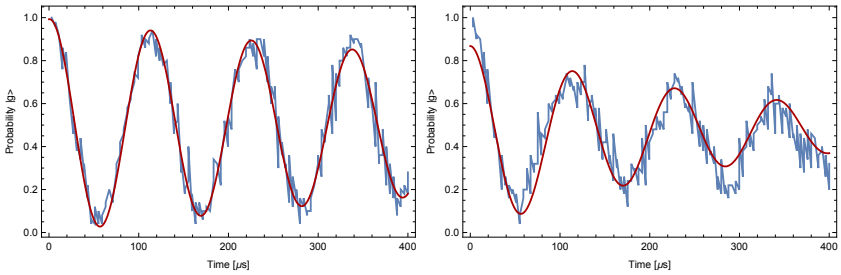

(a) Low Servo Gain, Servo Bumps at 0.6 MHz

(b) Medium Servo Gain, Servo Bumps at 1.5 MHz

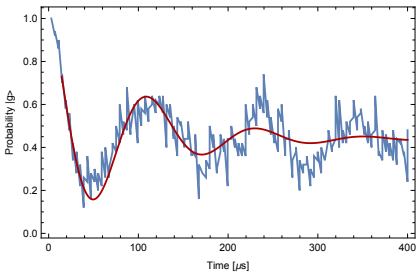

(c) High Servo Gain, Servo Bumps at 2.4 MHz

Figure 4.4.3: Rabi oscillations on the first blue sidebands with unfiltered light. With increasing gain values the contrast of the Rabi oscillations drops. The Rabi frequency inferred from the fit is $\approx 4.4\,\mathrm{kHz}$

is achieved, and the contrast for a single flop on the blue sideband was 0.80. With the filtered light $\tau = 1.2\,\mathrm{ms}$, and the contrast of a single flop on the blue sideband was 0.89.
The Rabi oscillations on the red sideband have the same frequency as the oscillations on the blue sideband, as the experiment is initiated with a carrier π pulse because no red sideband transition exists for the ground state. As a result for the red sideband the oscillation begins in the excited state (Fig. 4.4.6).
Comparing the frequency of oscillation on the sidebands to the frequency of the carrier, the Lamb Dicke parameter can be determined with a value of $\eta = 0.05$.

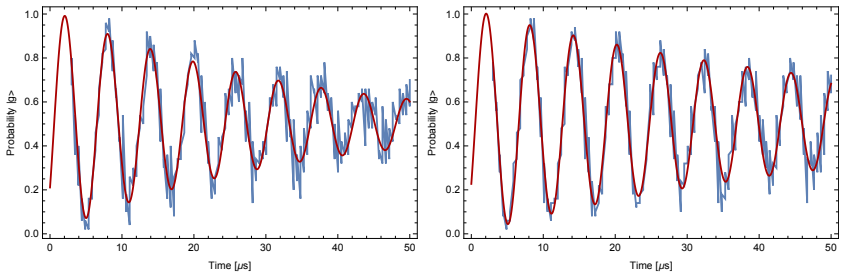

(a) Low Servo Gain, Servo Bumps at 0.6 MHz

(b) Medium Servo Gain, Servo Bumps at 1.5 MHz

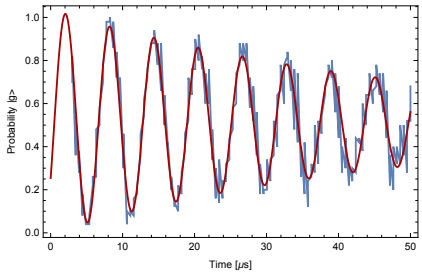

(c) High Servo Gain, Servo Bumps at 2.4 MHz

Figure 4.4.4: Rabi oscillations on the carrier transition with unfiltered light. For low gain values the contrast of the Rabi oscillations quickly drops.

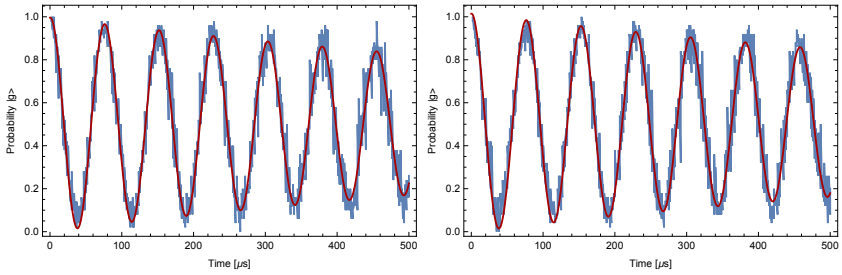

(a) Low Servo Gain

(b) High Servo Gain

Figure 4.4.5: Rabi oscillations on the first blue sidebands with filtered light. The Rabi frequency inferred from the fit is $\approx 6.5\,\mathrm{kHz}$

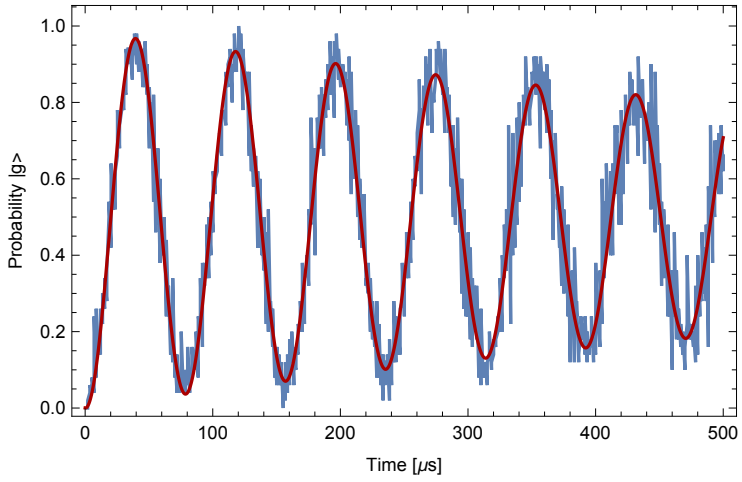

Figure 4.4.6: Rabi oscillations on the first red sidebands with filtered light. The Rabi frequency inferred from the fit is $\approx 6.4\,\mathrm{kHz}$

4.4.3 Mølmer-Sørensen gate

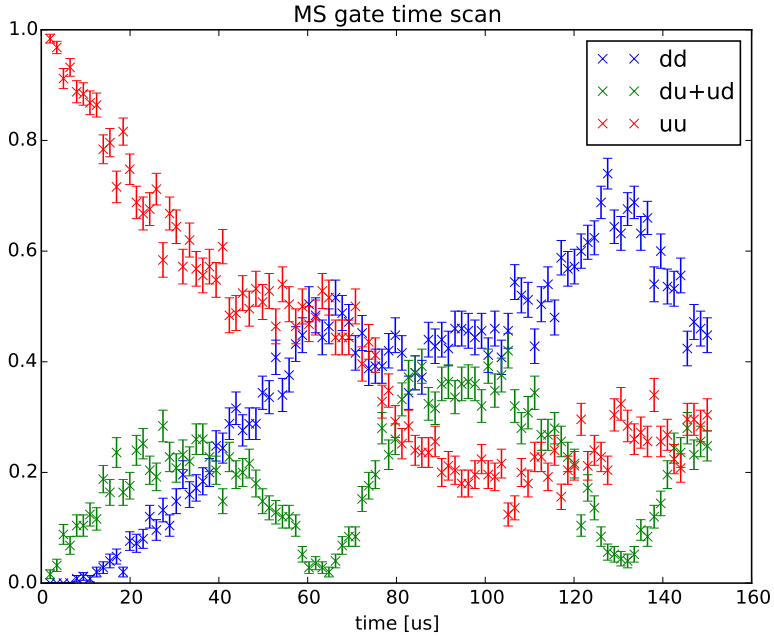

Figure 4.4.7: Time scan of a Mølmer-Sørensen gate. The two ions reach a maximally entangled state at $\approx 64\,\mu$s.

The spectrally filtered laser light could be used for implementing a two qubit Mølmer-Sørensen gate. After cooling and initialization a bichromatic beam was applied to both ions, with each component of the beam detuned by 16 kHz from the first red respectively blue sideband. Fig. 4.4.7 shows the evolution of the population. At $64\,\mu$s the probability of one bright ion and one dark one goes to 0 and the two ions are in the maximally entangled $|dd\rangle + i|uu\rangle$ state.
The maximally entangled state could be confirmed by a parity measurement (Fig. 4.4.8). Here a carrier pulse is applied, causing the system to oscillate between a superposition of the $|du\rangle$ and $|ud\rangle$ states and a superposition of the $|uu\rangle$ and $|dd\rangle$ states. The contrast of this oscillation gives a lower bound on the fidelity of the gate. A fidelity of 0.99 has been achieved.

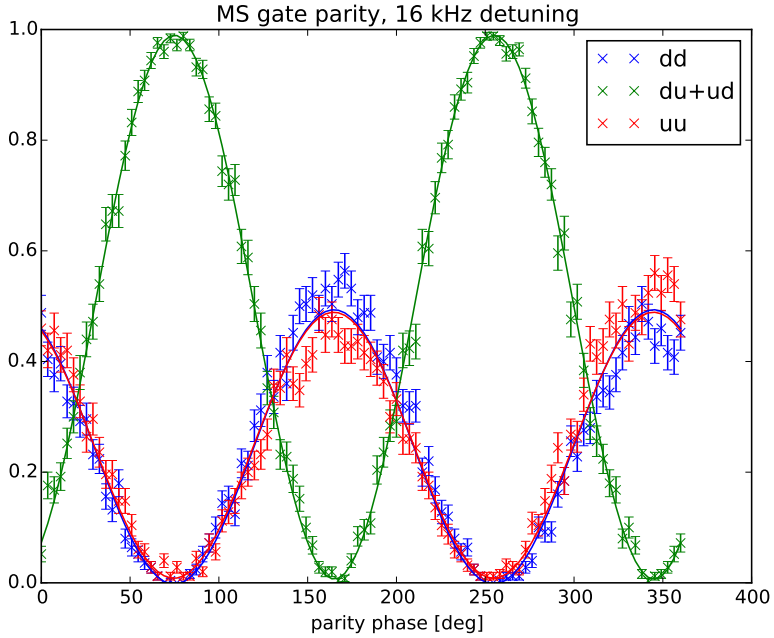

Figure 4.4.8: Parity measurement of the maximally entangled state.

Chapter 5

Conclusion

In order to perform qubit operations on $^{40}Ca^{+}$ with high fidelity a narrow linewidth laser at $\approx 729\,\mathrm{nm}$ is necessary. Locking the laser by PDH technique to a high finesse cavity can achieve the required stability, but the servo of the feedback loop causes additional spectral components in the laser spectrum offset from the center frequency by approximately the bandwidth of the controller. These servo bumps can significantly drive the carrier transition when the laser is detuned to a sideband.
In a first step a phase lock of the laser to a second narrow linewidth 729nm laser was set up to allow experiments to continue during this work.
In order to remove the servo bumps, the laser was locked to the high finesse cavity using an acousto-optic modulator. The cavity acts as an optical filter, and the servo bumps in the transmission signal are strongly suppressed.
The $\approx 40\,\mu\mathrm{W}$ strong transmission signal was then amplified by injecting a laser diode. The injection characteristics of two different diodes were investigated, and an amplification of the transmission to 45 mW was achieved while retaining the spectral purity.
The zero-crossing temperature of the high finesse cavity was measured, giving a result that is significantly lower than the value determined by a speed of sound measurement.

In a next step the light should be further amplified as currently after the losses by the fiber incoupling and the fiber noise setup only 17 mW arrive at the BoostTA system which amplifies the light for the experiment. This is less than the 30 mW the TA should be seeded with.
Further there are multiple experiments in the lab using $^{40}Ca^{+}$, all of which would benefit from using spectrally pure light. These experiments currently use the light from the TA output of TApro system, whos spectrum still has the servo bumps from the PDH lock.
One further diode per experiment could be injected with $\approx 1\,\mathrm{mW}$ each, outputting $40 - 50\,\mathrm{mW}$ which would be sufficient to properly seed a tapered amplifier.

Bibliography

[1] Richard P. Feynman. "Simulating physics with computers". English. In: *International Journal of Theoretical Physics* 21.6-7 (1982), pp. 467–488. ISSN: 0020-7748. DOI: 10.1007/BF02650179. URL: http://dx.doi.org/10.1007/BF02650179.

[2] Peter W Shor. "Algorithms for quantum computation: Discrete logarithms and factoring". In: *Foundations of Computer Science, 1994 Proceedings., 35th Annual Symposium on*. IEEE. 1994, pp. 124–134.

[3] Lov K Grover. "A fast quantum mechanical algorithm for database search". In: *Proceedings of the twenty-eighth annual ACM symposium on Theory of computing*. ACM. 1996, pp. 212–219.

[4] J. I. Cirac and P. Zoller. "Quantum Computations with Cold Trapped Ions". In: *Phys. Rev. Lett.* 74 (20 May 1995), pp. 4091–4094. DOI: 10.1103/PhysRevLett.74.4091. URL: http://link.aps.org/doi/10.1103/PhysRevLett.74.4091.

[5] David P DiVincenzo et al. "The physical implementation of quantum computation". In: *arXiv preprint quant-ph/0002077* (2000).

[6] Christian F. Roos. "Controlling the quantum state of trapped ions". PhD thesis. Universität Innsbruck, 2000.

[7] David J Wineland et al. "Experimental issues in coherent quantum-state manipulation of trapped atomic ions". In: *arXiv preprint quant-ph/9710025* (1997).

[8] M. Fox. *Quantum Optics : An Introduction*. Oxford Master Series in Physics. OUP Oxford, 2006. ISBN: 9780191524257.

[9] Anders Sørensen and Klaus Mølmer. "Quantum Computation with Ions in Thermal Motion". In: *Phys. Rev. Lett.* 82 (9 Mar. 1999), pp. 1971–1974. DOI: 10.1103/PhysRevLett.82.1971. URL: http://link.aps.org/doi/10.1103/PhysRevLett.82.1971.

[10] Anders Sørensen and Klaus Mølmer. "Entanglement and quantum computation with ions in thermal motion". In: *Phys. Rev. A* 62 (2 July 2000), p. 022311. DOI: 10.1103/PhysRevA.62.022311. URL: http://link.aps.org/doi/10.1103/PhysRevA.62.022311.

[11] Karin Fisher. "Coherent Control Laser System for the Quantum State Manipulation of Trapped Ions". MA thesis. ETH Zürich, 2013.

[12] Hsiang-Yu Lo. "Creation of Squeezed Schr¨oingers Cat States in a Mixed-Species Ion Trap". PhD thesis. ETH Zürich, 2015.

[13] K. Johan Aström and Richard M Murray. *Feedback systems: an introduction for scientists and engineers*. Princeton university press, 2010.

[14] Floyd M Gardner. *Phaselock techniques*. John Wiley & Sons, 2005.

[15] E. Hecht. *Optics*. Addison-Wesley World Student Series. Addison-Wesley, 1998. ISBN: 9780201304251.

[16] RWP Drever et al. "Laser phase and frequency stabilization using an optical resonator". In: *Applied Physics B* 31.2 (1983), pp. 97–105.

[17] Eric D Black. "An introduction to Pound–Drever–Hall laser frequency stabilization". In: *American Journal of Physics* 69.1 (2001), pp. 79–87.

[18] David R. Leibrandt et al. "Spherical reference cavities for frequency stabilization of lasers in non-laboratory environments". In: *Opt. Express* 19.4 (Feb. 2011), pp. 3471–3482. DOI: 10.1364/OE.19.003471. URL: http://www.opticsexpress.org/abstract.cfm?URI=oe-19-4-3471.

[19] Martin Sepiol. "Frequency stabilization of a 729 nm diode laser to an external high finesse reference cavity". MA thesis. ETH Zürich, Apr. 2012.

[20] Ludwig E. de Clercq. *EVIL Datasheet*. 2014. URL: http://www.qstarter.ch/wp-content/uploads/2014/04/EVIL.pdf (visited on 08/21/2015).

[21] Benjamin Keitch. "A quantum memory qubit in Calcium-43". PhD thesis. University of Oxford, 2007.

[22] Richard W. Fox. "Temperature analysis of low-expansion Fabry-Perot cavities". In: *Opt. Express* 17.17 (Aug. 2009), pp. 15023–15031. DOI: 10.1364/OE.17.015023. URL: http://www.opticsexpress.org/abstract.cfm?URI=oe-17-17-15023.

[23] H. E. Hagy and W. D. Shirkey. "Determining absolute thermal expansion of titania–silica glasses: a refined ultrasonic method". In: *Appl. Opt.* 14.9 (Sept. 1975), pp. 2099–2103. DOI: 10.1364/AO.14.002099. URL: http://ao.osa.org/abstract.cfm?URI=ao-14-9-2099.

[24] Christa Flühmann. "Stabilizing lasers and magnetic fields for quantum information experiments". MA thesis. ETH Zürich, Mar. 2014.

[25] *Vescent Laser Controller*. 2015. URL: http://www.vescent.com/manuals/doku.php?id=d2:laser_controller (visited on 08/28/2015).

[26] G.R. Hadley. "Injection locking of diode lasers". In: *Quantum Electronics, IEEE Journal of* 22.3 (Mar. 1986), pp. 419–426. ISSN: 0018-9197. DOI: 10.1109/JQE.1986.1072979.

[27] Alexander Hungenberg. "Improving Quantum Gate Fidelity Using Laser Intensity Based Post-Selection". MA thesis. ETH Zürich, June 2015.

[28] Long-Sheng Ma et al. “Delivering the same optical frequency at two places: accuratecancellation of phase noise introduced by an optical fiber or other time-varyingpath”. In: *Opt. Lett.* 19.21 (Nov. 1994), pp. 1777–1779. DOI: 10.1364/OL.19.001777. URL: http://ol.osa.org/abstract.cfm?URI=ol-19-21-1777.

[29] David B. Hume. “Two-Species Ion Arrays for Quantum Logic Spectroscopy and Entanglement Generation”. PhD thesis. University of Colorado, 2010.

[30] Matteo Marinelli. “High finesse cavity for optical trapping of ions”. MA thesis. ETH Zürich, 2014.

Appendix

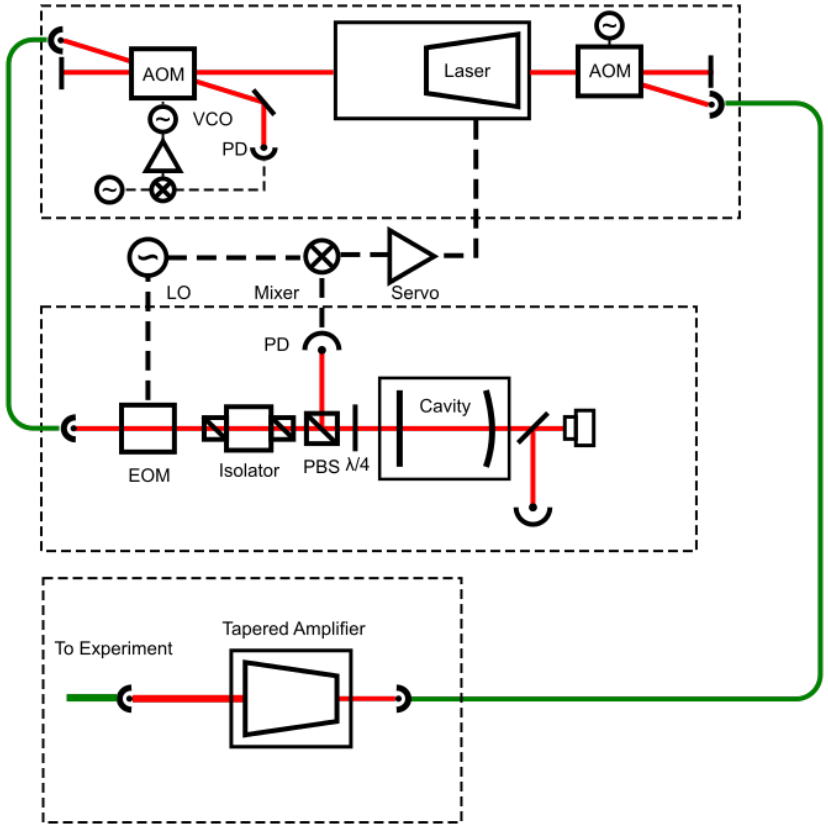

Figure .0.1: Original setup with the laser locked to the cavity by PDH lock

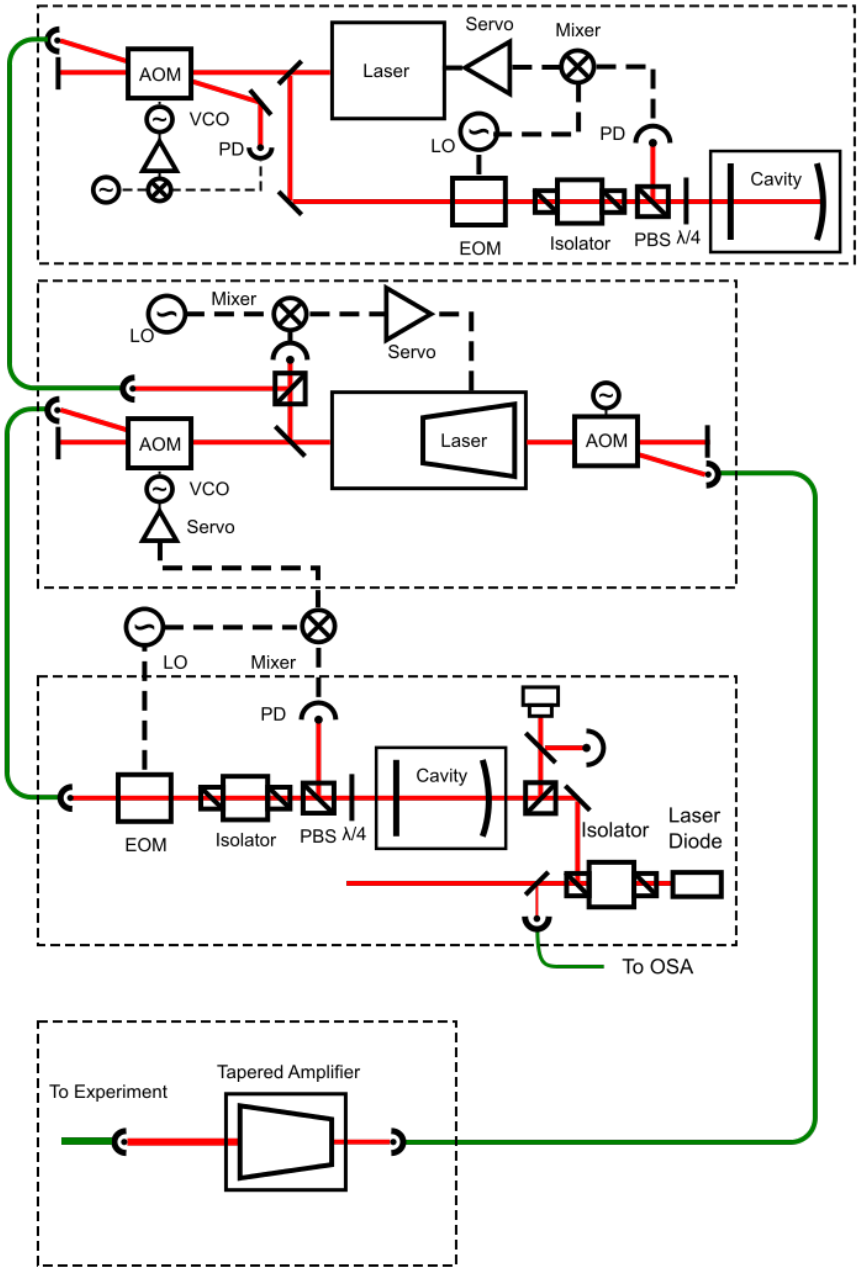

Figure .0.2: Intermediate setup. The laser is beat locked to a master laser, allowing work on the high finesse cavity without unlocking the laser.

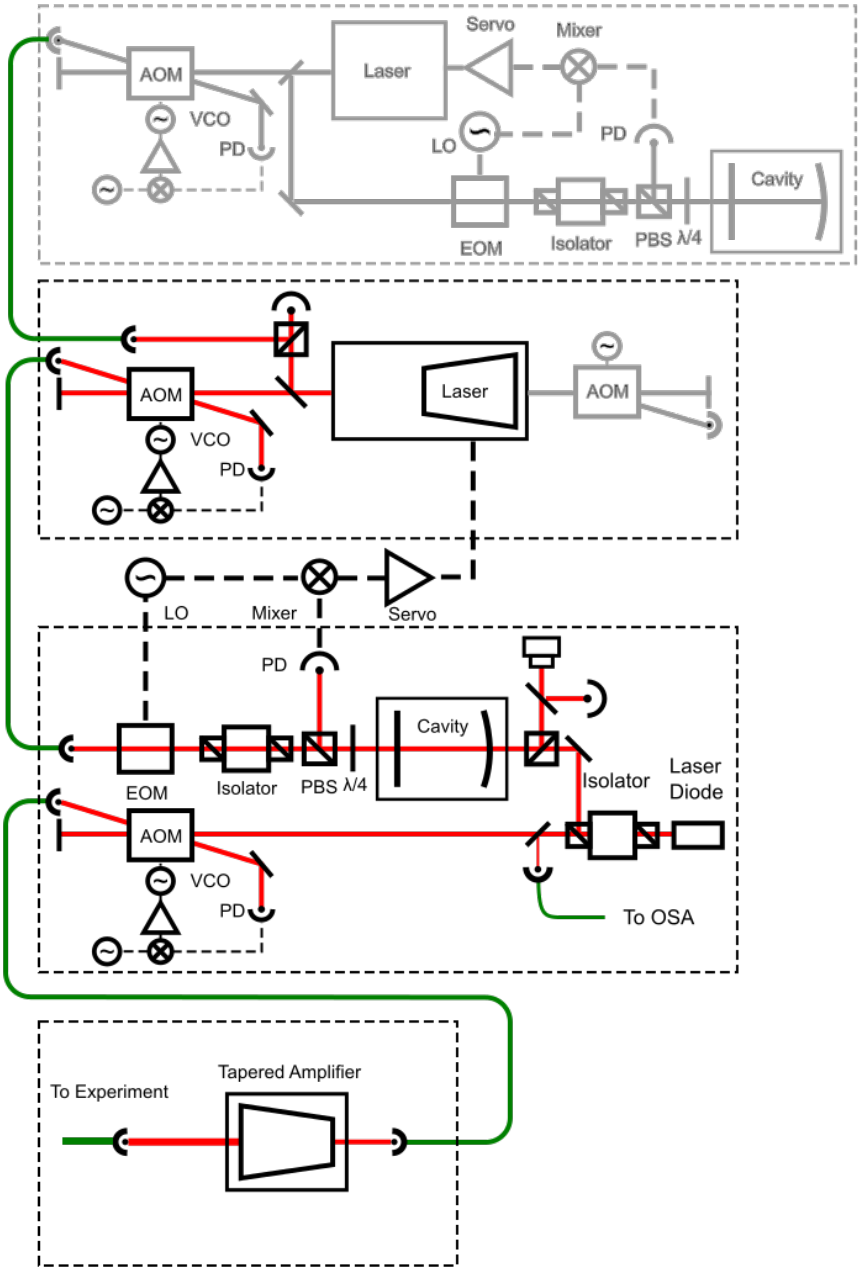

Figure .0.3: Final setup. The laser is again locked to the cavity, the amplified transmission signal is used for the experiment